High stress deformation and short-term thermal pulse preserved in exhumed lower crustal seismogenic faults (Lofoten, Norway)

Lucy Campbell[1] and Luca Menegon[2]

[1]University of Hull
[2]University of Oslo

November 21, 2022

Abstract

Seismic rupture in strong, anhydrous lithologies of the lower continental crust requires high failure stress, in the absence of high pore fluid pressure. Several mechanisms proposed to generate high stresses at depth imply transient loading driven by a spectrum of stress changes, ranging from highly localised stress amplifications to crustal-scale stress transfers. High transient stresses up to GPa magnitude are proposed by field and modelling studies, but the evidence for transient pre-seismic stress loading is often difficult to extract from the geological record due to overprinting by coseismic damage and slip. However, the local preservation of deformation microstructures indicative of crystal-plastic and brittle deformation associated with the seismic cycle in the lower crust offers the opportunity to constrain the progression of deformation before, during and after rupture, including stress and temperature evolution. Here, detailed study of pyroxene microstructures characterises the short-term evolution of high stress deformation and temperature changes experienced prior to, and during, lower crustal earthquake rupture. Pyroxenes are sampled from pseudotachylyte-bearing faults and damage zones of lower crustal earthquakes recorded in the exhumed granulite facies terrane of Lofoten, northern Norway. The progressive sequence of microstructures indicates localised high-stress (at the GPa level) preseismic loading accommodated by low temperature plasticity, followed by coseismic pulverisation-style fragmentation and subsequent grain growth triggered by the short-term heat pulse associated with frictional sliding. Thus, up to GPa-level transient high stress leading to earthquake nucleation in the dry lower crust can occur in nature, and can be preserved in the fault rock microstructure.

High stress deformation and short-term thermal pulse preserved in exhumed lower crustal seismogenic faults (Lofoten, Norway)

L. R . Campbell[1*] & L. Menegon[2]

[1]Department of Geography, Geology and Environment, University of Hull, Hull HU6 7RX

[2]The Njord Centre, Department of Geosciences, University of Oslo, P.O. Box 1048, Blindern, Norway

*Corresponding author email: l.r.campbell@hull.ac.uk

Key Points

- Localised differential stresses exceeding 1 GPa during pre-seismic loading accommodated in dislocation glide of pyroxenes.
- Microstructures capable of recording transient stress changes prior to and during seismic rupture in the lower crust.
- Coseismic deformation represented by pulverisation-style fragmentation and thermally activated grain growth within orthopyroxene.

Abstract

Seismic rupture in strong, anhydrous lithologies of the lower continental crust requires high failure stress, in the absence of high pore fluid pressure. Several mechanisms proposed to generate high stresses at depth imply transient loading driven by a spectrum of stress changes, ranging from highly localised stress amplifications to crustal-scale stress transfers. High transient stresses up to GPa magnitude are proposed by field and modelling studies, but the evidence for transient pre-seismic stress loading is often difficult to extract from the geological record due to overprinting by coseismic damage and slip. However, the local preservation of deformation microstructures indicative of crystal-plastic and brittle deformation associated with the seismic cycle in the lower crust offers the opportunity to constrain the progression of deformation before, during and after rupture, including stress and temperature evolution.

Here, detailed study of pyroxene microstructures characterises the short-term evolution of high stress deformation and temperature changes experienced prior to, and during, lower crustal earthquake rupture. Pyroxenes are sampled from pseudotachylyte-bearing faults and damage zones of lower crustal earthquakes recorded in the exhumed granulite facies terrane of Lofoten, northern Norway. The progressive sequence of microstructures indicates localised high-stress (at the GPa level) preseismic loading accommodated by low temperature plasticity, followed by coseismic pulverisation-style fragmentation and subsequent grain growth triggered by the short-term heat pulse associated with frictional sliding. Thus, up to GPa-level transient high stress leading to earthquake nucleation in the dry lower crust can occur in nature, and can be preserved in the fault rock microstructure.

Plain language summary

Earthquake initiation within strong, dry rock types in the lower continental crust requires high driving stresses, if fluids are absent. There are several methods proposed to generate these unusually high stresses at lower crustal depths, many implying very short-term stress increases. High short-term stresses up to GPa magnitudes are proposed by the results of fieldwork and numerical modelling, but the geological record for these stress increases occurring in the build-up to earthquakes is not always clear due to the subsequent earthquake deformation overwriting any previous microstructures. However, locally, a complete record of stress change before, during and after an earthquake may be preserved.

Here, a detailed study of pyroxene deformation microstructures characterises the short-term changes in stress and temperature experienced prior to, and during, lower crustal earthquakes. Pyroxene crystals close to faults exhibiting ancient earthquake-generated frictional melts (pseudotachylytes) are investigated from an exhumed shear zone in Lofoten, northern Norway. The microstructures imply high stress loading prior to the earthquake, followed by pervasive fragmentation and subsequent grain growth linked to the passage of the earthquake rupture. These results support GPa magnitude stresses localised in the lower crust and show that microstructures are capable of preserving these short term changes.

1. Introduction

Relocations of focal mechanisms and increased recognition of the geological signature of earthquakes recorded in exhumed lower crustal terranes have promoted the exploration of a number of models for nucleating seismic rupture within otherwise typically viscous deformation regimes. Many of these models require stress amplification or transfer, whether driven by local rheological heterogeneities across a shear zone network (Orlandini & Mahan, 2020; Campbell *et al.* 2020, Hawemann *et al.* 2019), dehydration reactions that increase fluid pressure (Hacker et al., 2003) or locally redistribute stress (Ferrand et al., 2017), or downdip stress loading from seismogenic activity shallower in the crust (Jamtveit et al., 2018; Dunkel et al., 2020; Papa et al., 2020; Ellis & Stöckhert, 2004). Intracrystalline deformation and recrystallisation occurring over geologically rapid timescales (i.e. equivalent to the seismic cycle) has been previously recognised in fault zones and deformation experiments (Bestmann et al., 2012; Campbell & Menegon, 2019; Kidder et al., 2016), and recent work on both naturally and experimentally deformed mid- to lower- crustal rocks has linked similar microstructures to transient variations in stress. In some cases, such microstructures can be clearly linked to localised stress amplifications associated with deep crustal earthquakes, whether stress increases were generated in-situ within the lower crust (Anderson et al., 2021; Campbell et al. 2020; Hawemann et al., 2019) or were transferred from shallower crustal levels (Papa et al., 2020; Ellis & Stöckhert, 2004; Trepmann & Stöckhert, 2013; Trepmann & Stöckhert, 2002). In both cases the stress amplification can be significant (e.g. 100s MPa, Ellis & Stöckhert 2004), but earthquake nucleation in the lower crustal may require stresses on the order of GPa, especially within strong, anhydrous granulite terranes in the absence of high pore fluid pressure. Such stress magnitudes have recently been captured in mica kink-bands linked to pre-seismic stress accumulation (Anderson et al. 2021) and implied by field characterisation of pseudotachylyte-bearing faults (Campbell et al., 2020). The ability of microstructures to capture progressive and transient stress variation throughout the earthquake cycle (Brückner & Trepmann, 2021; Anderson et al, 2021, Campbell & Menegon, 2019, Petley-Ragan et al., 2019) offers an under-explored opportunity to further investigate deformation mechanisms and conditions associated with stress amplification and rupture in the lower crust.

We present here a microstructural study of lower crustal pseudotachylyte-bearing faults that seeks to constrain the timing and magnitude of stresses associated with the nucleation and propagation of seismic rupture in the lower crust, as well as the corresponding sequence of deformation processes. Following work on deformation of plagioclase (e.g. Soda and Okudaira, 2018; Petley-Ragan et al., 2018, 2021) and garnet (Austrheim et al., 2017; Petley-Ragan et al., 2019; Hawemann et al, 2019;

Papa et al., 2018) in lower crustal seismogenic faults, we focus on the deformation microstructures of pyroxenes, which present a clearer record relative to plagioclase of overprinting and spatial association of deformation with localised faulting in our samples. By studying orthopyroxene and clinopyroxene both from the margins of, and as unmelted survivor clasts within granulite-facies pseudotachylyte-bearing faults, we are able to propose a record of spatial and temporal stress and temperature variation related to the seismic cycle in the lower continental crust.

2. Geological context

We investigate pseudotachylyte samples from the Flakstadøy anorthosite near Nusfjord, Lofoten, Norway. This anorthosite body forms part of the Anorthosite-Mangerite-Charnockite-Granite (AMCG) suite, intruded into the lower crust of the Baltic Shield around 1.9-1.7 Ga at granulite facies conditions (Corfu, 2004). The well-preserved coarse-grained igneous texture and mineralogy of the Flakstadøy anorthosite consists of plagioclase + minor amounts of clinopyroxene ± amphibole ± quartz ± orthopyroxene ± garnet ± biotite (Markl et al., 1998; Menegon et al., 2017). The anorthosite can be considered anhydrous, containing ca. 0.04 wt. % H_20 and no free H_2O at the time of deformation (Menegon et al., 2017).

Within the Flakstadøy anorthosite, a network of thin shear zones (usually 1 – 30 cm in width) cut across the intrusion, occurring in three dominant orientations (Menegon et al., 2017) and dividing up the anorthosite into a series of low strain blocks (Fig. 1a). In turn, these blocks are cut by pseudotachylyte-bearing faults (Fig. 1b), indicating episodic seismic failure ('type-2' pseudotachylytes of Campbell et al., 2020). The surrounding anorthosite, whilst fractured, also typically shows very limited evidence of viscous creep away from either the shear zones or the pseudotachylyte veins (Fig. 1c). The transient high stresses required to trigger seismic failure within these blocks were interpreted to result from localised stress amplifications driven by activity along the viscously deforming shear zones (Campbell et al., 2020). Therefore, the seismicity recorded by these 'type-2' pseudotachylytes nucleated at ambient conditions of the coeval shear zone deformation, 650-750 °C and 0.7-0.8 GPa (Menegon et al., 2017), implying depths of 25 – 30 km in the continental lower crust. These 'type-2' pseudotachylyte veins (Fig. 1d) show very limited overprinting by viscous reactivation, preserving primary quench crystallisation morphologies (e.g. radiating microlites, spherulites, dendritic crystals) and chilled margins (Fig. 1d, e). In this contribution, we look for the microstructural evidence to constrain potential GPa levels of preseismic loading suggested by Campbell et al. (2020), and identify further coseismic rapid stress and temperature oscillations.

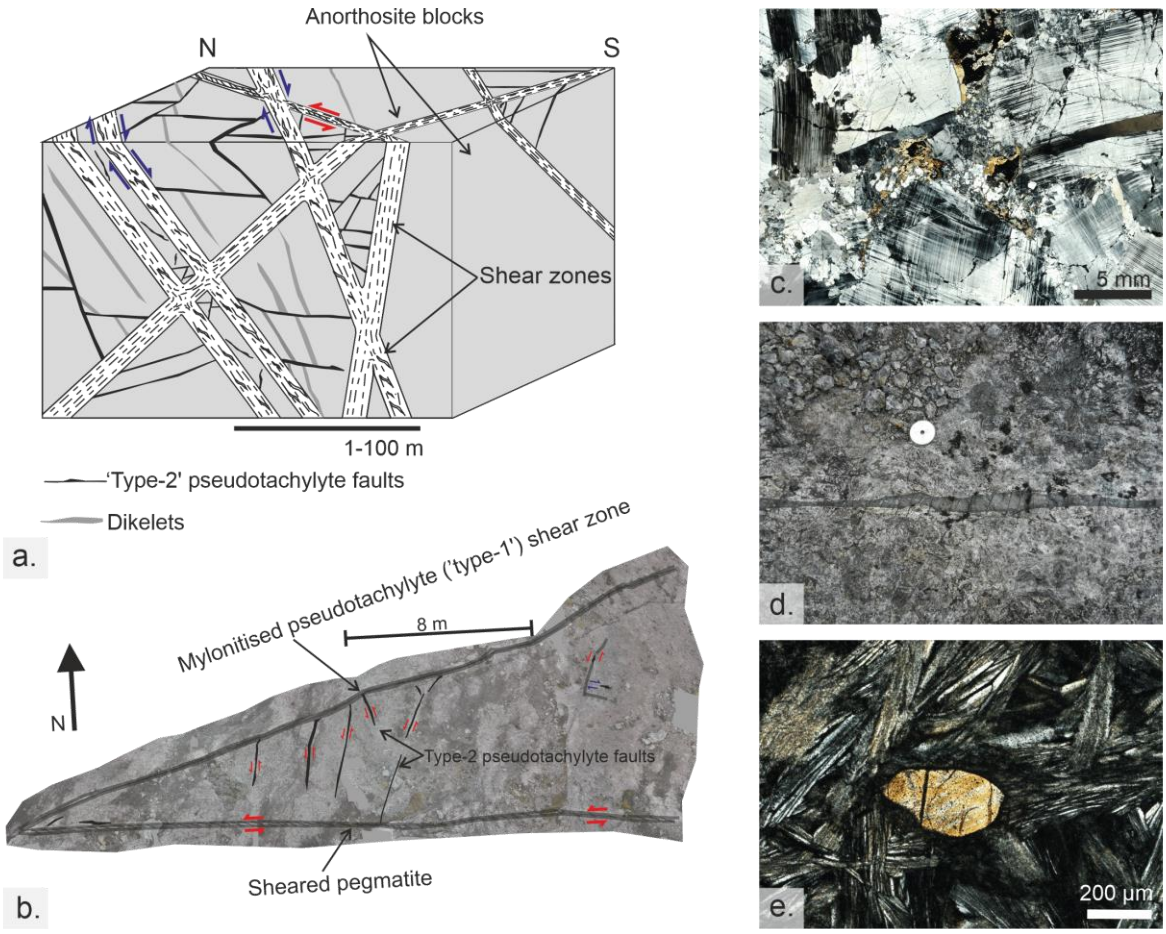

Figure 1. *Pseudotachylytes representing lower crustal earthquake nucleation associated with viscous creep along active shear zone networks near Nusfjord, Lofoten.* ***a)*** *Block diagram showing pseudotachylyte faults that dissect low-strain anorthosite blocks between localised viscous shear zones;* ***b)*** *map of faults and shear zones across one such block in the Flakstadøy anorthosite (68.055°N 13.367°E);* ***c)*** *typical form of anorthosite within shear-zone bounded blocks at distance from pseudotachylyte faults (cross-polarised image).* ***d)*** *example of pseudotachylyte fault with chilled margin, located in block shown in b) (68.055°N 13.367°E);* ***e)*** *Orthopyroxene clast in crystalline matrix of pseudotachylyte showing characteristic radiating plagioclase microlites (cross-polarised image).*

3. Methods

3.1 Microstructural analysis and electron backscatter diffraction (EBSD)

Polished thin sections of samples of pseudotachylyte veins were cut perpendicular to the vein wall but the slip directions remain unconstrained. Thin sections were analysed using a combination of light and scanning electron microscopy (SEM). SEM data were acquired at the Electron Microscopy Centre at the University of Plymouth using a JEOL 7001 FEG-SEM and a JEOL 6610 low vacuum SEM. Typical beam conditions were 10-13 nA probe current and 20 kV accelerating voltage.

Samples for electron backscatter diffraction (EBSD) analysis underwent additional preparation with colloidal silica polishing and carbon coating. Data were acquired at the Electron Microscopy Centre at the University of Plymouth using a JEOL 7001 FEG-SEM and a JEOL 6610 low vacuum SEM, equipped with an Oxford Instruments Nordlys Nano and a Nordlys Max detector, respectively. During EBSD analysis, working distances were set up between 15.2 mm and 24.2 mm, accelerating voltage was 20 kV and the sample was tilted at 70°. Step sizes for EBSD mapping ranged from 0.1 µm to 0.9 µm. Phases were indexed using AZtec (Oxford Instruments) acquisition software. Processing was undertaken with Channel 5 (Oxford Instruments) software. Filtering of the raw data involved removing wild spikes, nearest neighbour extrapolation and removal of any grains with circle-equivalent diameters less than three times the step size. The results are presented in the form of phase maps, orientation maps (inverse pole figure, IPF, maps), grain orientation spread (GOS) maps, showing the average misorientation of a grain with respect to that grain's mean orientation, grain reference orientation deviation (GROD) maps, showing the misorientation of points relative to that grain's mean orientation, and texture component (TC) maps showing the misorientation with respect to a chosen point in a given grain. Pole figures (lower hemisphere, equal angle) and maps are orientated with respect to the pseudotachylyte vein and pole figures show a reference frame perpendicular (Z_v) and parallel (X_v) to the vein edge.

3.2 Boundary trace analysis

Identification of slip systems using EBSD analysis was undertaken using the boundary trace analysis (BTA) technique. Using this method, subsetted regions transecting low-angle boundaries (with misorientation in the 2-9° range) were created from EBSD orientation maps. Pole figures were created for each subset. The BTA method assumes a tilt boundary model, where the two regions each side of the boundary are rotated around an axis parallel to the boundary plane. This axis, providing it is parallel to a crystal axis, will be represented in the pole figure by a tight point cluster at the position of that axis, whilst the other crystal axes may show rotation around that orientation via a dispersed smear of points. The slip plane can be identified as it must contain both the rotation axis and the slip direction, and the slip direction along with the pole to the slip plane must lie in a plane that is perpendicular to the rotation axis (Lloyd et al., 1997).

3.3 Image analysis for gain size distributions

Analysis of grain size distributions of fine-grained pyroxene aggregates occurring in the damage zone of and in survivor clasts within type-2 pseudotachylytes was undertaken using the freely available image analysis software 'ImageJ'. Grain boundaries were identified via segmentation of SEM backscatter electron (BSE) images acquired at magnification ranging from 850x to 2300x. Grain area and circle equivalent diameter (D_{equ}) were then measured and calculated with ImageJ.

4. Results

4.1 Sample description

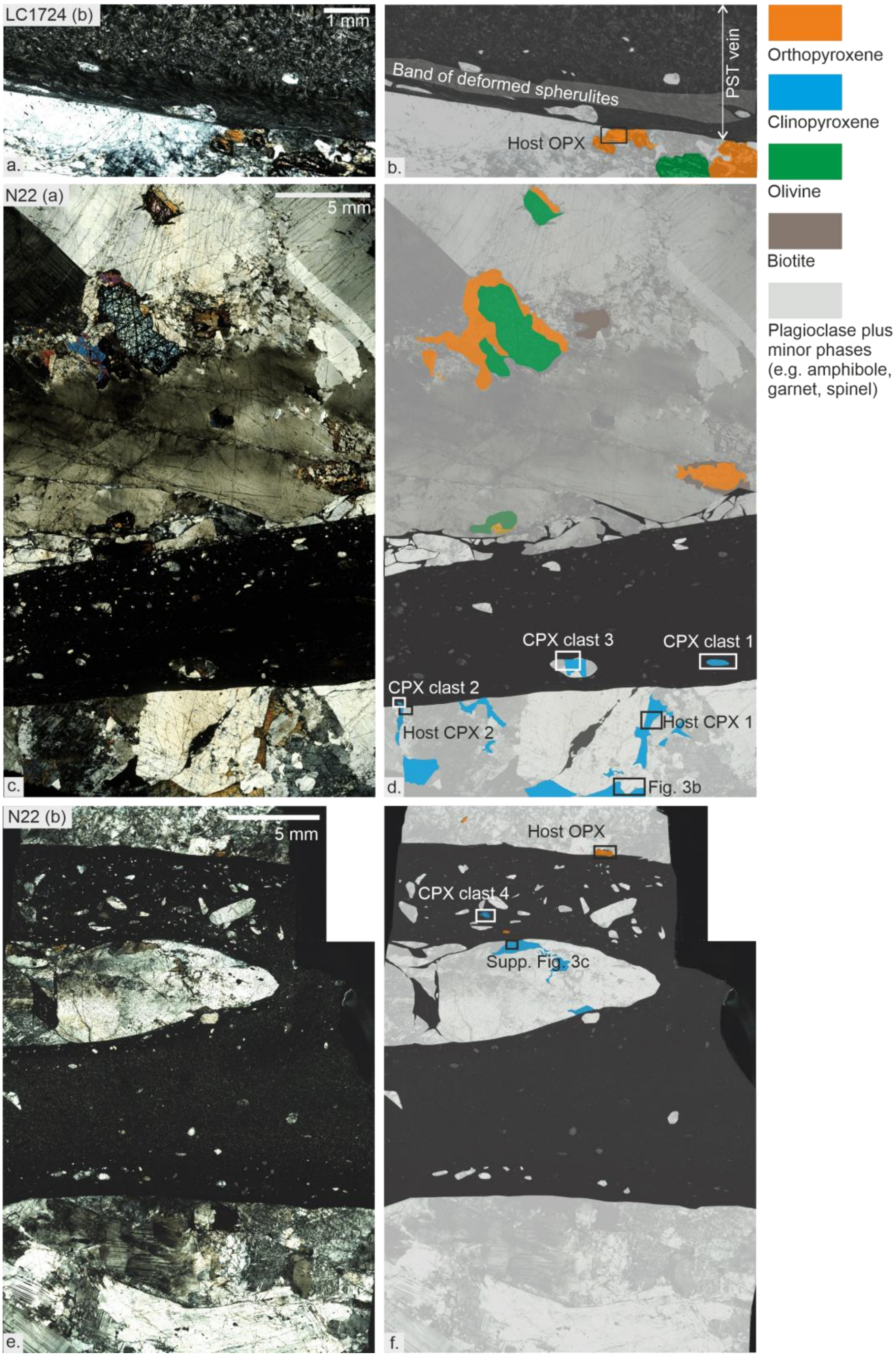

***Figure 2**. Distribution of pyroxenes and other phases in association with pseudotachylyte veins (blue = clinopyroxene; orange = orthopyroxene; green = olivine). Areas analysed in this work are labelled; **a)** pseudotachylyte fault vein and anorthosite host rock in sample LC1724. (Only one side of the fault is captured – the margin of this pseudotachylyte vein has a 1 mm thick band of sinistrally sheared spherulitic structures (cross-polarised light, thin section 'b'); **b)** overlay highlighting mineralogy of a); **c)** pseudotachylyte fault vein cutting anorthosite in sample N22 (cross-polarised light, thin section 'a'); **d)** overlay highlighting mineralogy in c); **e)** Thin section N22b (cross-polarised light) showing pseudotachylyte vein and clasts; **f)** overlay showing mineralogy of e).*

Pyroxenes are described from two pseudotachylyte veins: LC1724 (Figs. 2a-b) and N22 (Figs. 2c-f).

These veins consist of pristine, unaltered pseudotachylyte that preserves quench crystallisation morphologies of the coseismic melt, such as chilled margins, radiating microlites and spherulites (Figs. 1e, 2). In sample LC1724, a restricted viscous shear deformation is observed in the fine-grained pseudotachylyte margin (Fig. 2a). However, this viscous creep was spatially highly restricted to a zone < 1 mm wide adjacent to the margin, and has not deformed the fault walls of the anorthosite.

Samples N22 and LC1724 belong to two different networks of short (< 15 m long) type-2 pseudotachylyte-bearing faults developed in decametric pods of undeformed anorthosite bounded by ductile shear zones (see Campbell et al. 2020). N22 was sampled from 68.054°N 13.361°E and LC1724 from 68.056°N 13.377°E. Neither record unambiguous evidence for the sense of slip. The anorthosite host rock in these samples consists of plagioclase (labradorite), clinopyroxene (diopside) and orthopyroxene (enstatite), with minor amounts of olivine, hornblende, biotite, pleonaste spinel, and garnet (Fig. 2). Olivine is mostly altered to iron oxides and enstatite, and is locally rimmed by coronas of intergrown enstatite, pleonaste spinel, hornblende and biotite. Garnet may rim orthopyroxene in contact with plagioclase.

The microcrystalline matrix of the LC1724 pseudotachylyte is primarily composed of plagioclase (labradorite), orthopyroxene (enstatite) and clinopyroxene (diopside). Locally the pseudotachylyte matrix may also contain biotite, potassium feldspar and hornblende. The pseudotachylyte vein displays radiating microlites of plagioclase in the centre of the vein, becoming finer and more granular towards the margin (Figs. 1e, 2a). Survivor clasts observed in this sample are composed predominantly of plagioclase and orthopyroxene. The margin with the host rock is planar and has no significant injection features visible within the thin section. The pseudotachylyte vein is 11 mm thick.

The microcrystalline matrix of the N22 pseudotachylyte is composed of plagioclase (andesine), orthopyroxene (enstatite), clinopyroxene (diopside), hornblende and minor biotite (see Menegon et al. (2017) for XRF analysis of sample N22). Survivor clasts are typically of plagioclase, orthopyroxene, clinopyroxene and some apatite. A damage zone containing fragmented wall rock surrounded by thin veins of pseudotachylyte extends for around 2 mm preferentially on one side of the main vein (Figs. 2c,d). An additional sample of the N22 vein displays a large, cm-scale fragmented lithic clast with an internal network of thin pseudotachylyte veins connected to the main vein (Fig. 2e). The main pseudotachylyte vein has a maximum thickness of 18 mm.

4.2 Microstructure of clinopyroxene

4.2.1. Host rock

Across the undeformed host rock, clinopyroxene grains display orthopyroxene lamellae. In the anorthosite internal blocks between shear zones (Fig. 1a), clinopyroxene only rarely has twins evident (Fig. 3a) but twinning becomes present close to pseudotachylyte veins (Fig. 3b) at distances of < 2cm (i.e. within a thin section).

EBSD maps of an elongate clinopyroxene grain (Fig. 2d, 'host CPX 1') lying 1-2 mm away from the N22 pseudotachylyte fault vein margin indicate laminar and slightly discontinuous twinning on (001) and to some extent on (100) planes (Figs. 3c-e). (001) twins are cut by a probable fracture, represented as a low-angle boundary (LAB) in Fig. 3c. Lamellae of orthopyroxene also lie along (100) planes of clinopyroxene. The grain orientation spread (GOS) of the clinopyroxene grain is < 5°, and is lowest within the twins (Fig. 3d). Clinopyroxene in the immediate margin to the fault (Fig. 2d, 'host CPX 2'), and cut by the pseudotachylyte vein, shows laminar (001) twinning (Fig. 3f-h). The GOS of the clinopyroxene grain here is variable but always < 4° and again is lowest in the twin lamellae (Fig. 3g). Although the IPF (Z) map is fairly uniform, grain reference orientation deviation (GROD) maps pick out subtle undulations parallel to (001) (Supp. Fig. 1a).

4.2.2 Clasts in pseudotachylytes

All survivor clasts of clinopyroxene display twinning on (100) and orthopyroxene lamellae along (100) (Figs. 4,5). Clast 1 (Fig. 2d, 'clinopyroxene clast 1') is the most obviously elongate in shape (Fig. 4), measuring approximately 1000 x 300 µm, but all other clasts appear slightly elongate parallel to the vein margin except for clast 3, where the clinopyroxene forms part of a lithic clast alongside plagioclase (Fig. 2d, 'CPX clast 3'). (100) is typically parallel or sub-parallel to the vein margin in clasts 1 and 3-4. Clast 1, and to some extent clast 4 (Fig. 2f 'CPX clast 4'), are bent, visible in the curvature of orthopyroxene lamellae (Fig. 4, 5c).

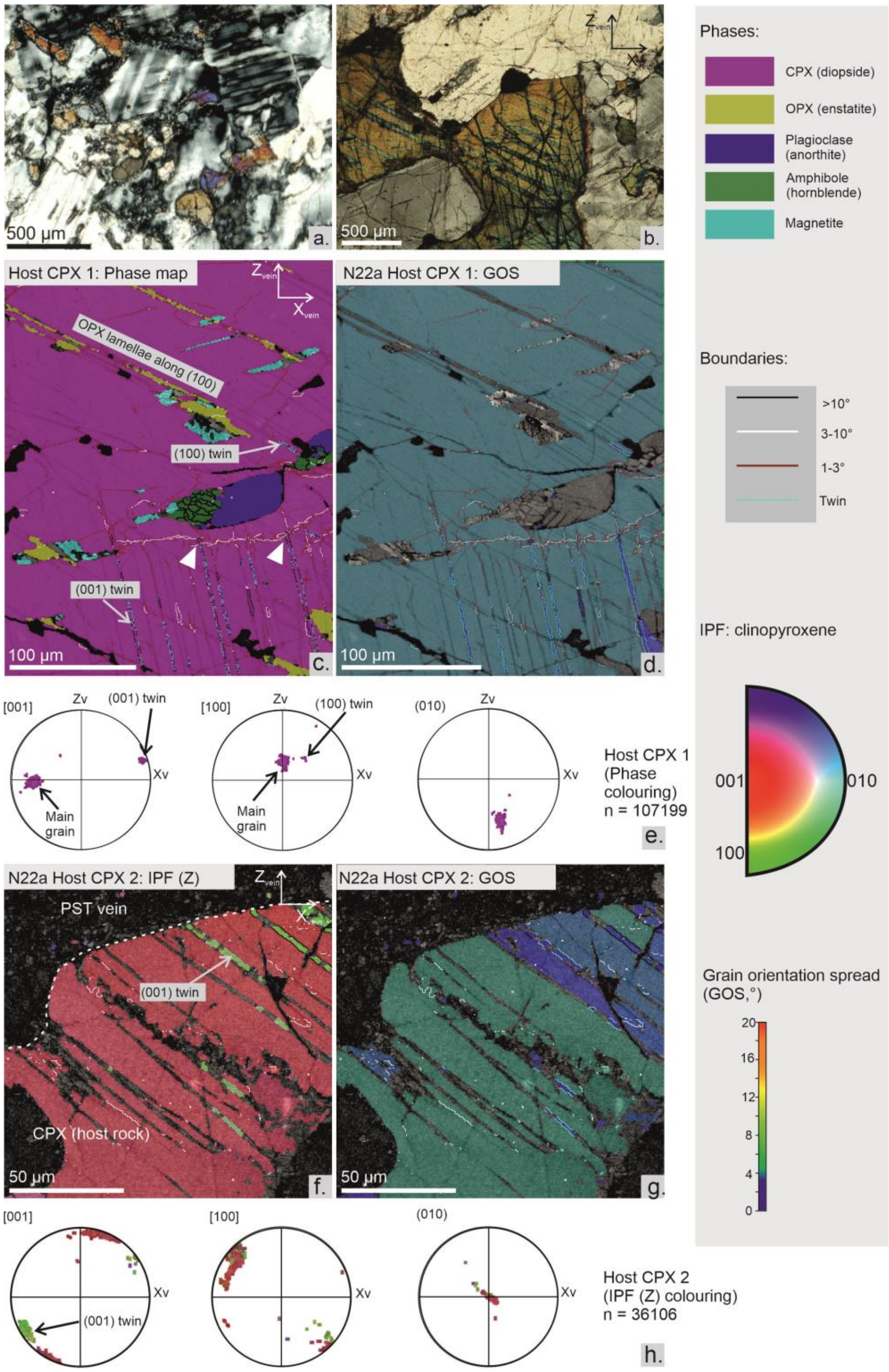

Figure 3. *Microstructures of clinopyroxene in the host anorthosite;* ***a)*** *fine-grained clinopyroxene in anorthosite sampled within a shear-zone bounded block but away from any faults – shows detail of Fig. 1c (cross-polarised light);* ***b)*** *clinopyroxene situated 5 mm from vein edge (position indicated in Fig. 2d) showing twinning (cross-polarised image);* ***c)*** *EBSD phase map of clinopyroxene situated 2 mm from vein edge (position indicated in Fig. 2d, 'Host CPX 1') showing orthopyroxene lamellae, twin boundaries, and scarce low angle boundaries which truncate twining (white arrowheads);* ***d)*** *grain orientation spread (GOS) map across same host rock clinopyroxene with values < 5°, indicating low internal strain;* ***e)*** *pole figures for host clinopyroxene 1 as shown in c) with phase colouring* ***f)*** *IPF (Z) map of clinopyroxene in the immediate margin of the pseudotachylyte (position indicated on Fig. 2d, 'Host clinopyroxene 2') showing little change in orientation across the grain;* ***g)*** *GOS map of same clinopyroxene grain showing very little internal strain;* ***h)*** *pole figures for host clinopyroxene 2 as shown in f) with IPF(Z.)*

Clasts 1 and 4, plus regions near the edges of clasts 2 and 3 (Figs. 2a, b) show moderately high GOS

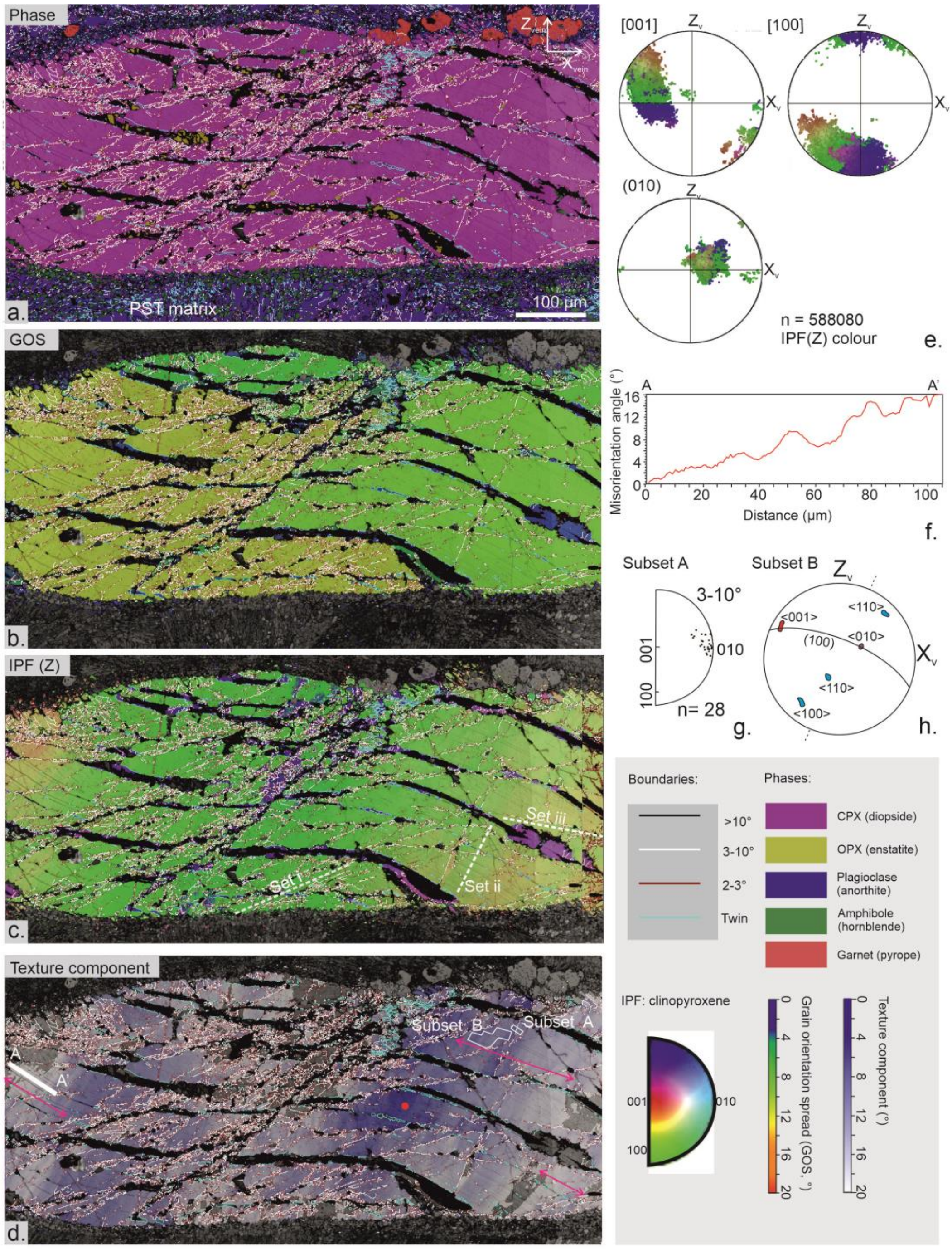

Figure 4. *Microstructure of clinopyroxene clast '1' from EBSD analysis (position shown in Fig. 2d);* ***a)*** *Phase map highlighting bent orthopyroxene lamellae, twin boundaries and low angle boundaries;* ***b)*** *GOS map illustrating variable, but moderate, internal strain across the clinopyroxene grain. Twin lamellae have very low (blue) values;* ***c)*** *IPX (Z) orientation map of clinopyroxene. Lattice distortion of the entire grain is clear, as are twinned regions. Sets of low angle boundary orientations are labelled;* ***d)*** *texture component map (for clinopyroxene only) showing degrees of misorientation away from the reference point (red circle)***.** *Smaller-wavelength undulations are most easily seen here, strongly developed over regions indicated by pink arrows;* ***e)*** *pole figures (lower hemisphere) for [001] and [100] axes and poles to (010) planes of clast 1;* ***f)*** *misorientation profile from A-A' (location indicated in d.) showing regular 20-40 µm undulation of the lattice. The progressive increase in misorientation from point A is due to the long wavelength kinking of the clast;* ***g)*** *Rotation axes shown in crystal co-ordinates and crystal axes shown in sample co-ordinates for subset A, indicated in d.);* ***h)*** *pole figures for undulating region 'subset B' (indicated in d.), used for boundary trace analysis. The rotation axis [010] is indicated in purple and the suggested slip direction in red. The boundary trace parallel to the periodic undulation is indicated by the dashed lines.*

up to 12° (Fig. 4b, 5d-e). Lower GOS values are seen within twins and within orthopyroxene lamellae, and the lowest values occur where the orthopyroxene lamellae have recrystallized into a polycrystalline aggregate. Clasts 1, 3, and 4 show systematic undulations with amplitudes of low misorientation (< 4°) with wavelengths typically of 20-40 μm, which are most evident on texture component maps in regions free from twinning and low angle boundaries (Figs. 4d, 5f). These features continue into the orthopyroxene lamellae. The change in orientation across these undulations is continuous (Figs 4f, 5g) and we use the term 'periodic undulations' to refer to these. The boundary trace analysis in clast 1 indicates that the undulations, as well as low-angle boundaries parallel to them, are the result of slip on the [001](100) system with [010] as rotation axis (Fig. 4g,h). However, the undulations in clast 4 do not give a clear rotation axis for boundary trace analysis, though there is some clustering around [001] (Fig. 5h).

Low-angle boundaries are developed in different orientations, most clearly seen in clast 1 which has three recognisable sets ('i-iii': Fig. 4c). Set (i) LABs cut and offset the orthopyroxene lamellae and the periodic undulations. Clast 4 also has prominent linear LABs with some common orientations (Fig. 5c). As in clast 1, some linear LABs cut the undulations and offset sharply the orthopyroxene lamellae (Fig. 5f).

Fine-grained clinopyroxene occurs in intracrystalline bands across some clasts. In clast 2, fine-grained clinopyroxene has D_{equ} of 1.8-8.2 μm (Fig. 5a), and shows similar but dispersed orientations relative to the parent clast (Supp. Fig. 2a-b). Rotation axes of these smaller grains are scattered and do not clearly cluster around crystallographic rotation axes. The intracrystalline bands may also contain hornblende (Fig. 5a), they crosscut some LABs (Fig. 5a), and they generally offset orthopyroxene lamellae sharply. Clast 3 contains a similar example of a prominent intracrystalline band with a width up to 15 μm (Fig. 5b). Fine-grained clinopyroxene in this band has a dispersed CPO relative to the rest of the clast (Supp. Fig. 2c-d). Orthopyroxene lamellae, clinopyroxene twin boundaries and any LABs are truncated and offset across the band. The band contains fine-grained clinopyroxene alongside garnet and hornblende (Fig. 5). Both are also fine-grained (2-20 μm), although the garnet coarsens at the edge of the mapped region, on the rim of the clinopyroxene grain. This assemblage shows no sign of retrograde metamorphic reactions. Similar bands in clinopyroxene filled with fine-grained clinopyroxene and amphibole were described from the proximal damage zone of Nusfjord type-2 pseudotachylytes in Jamtveit et al. (2019), and were interpreted as intracrystalline fractures that localized mineral reactions and phase nucleation.

4.3 Microstructure of orthopyroxene

4.3.1 Host rock

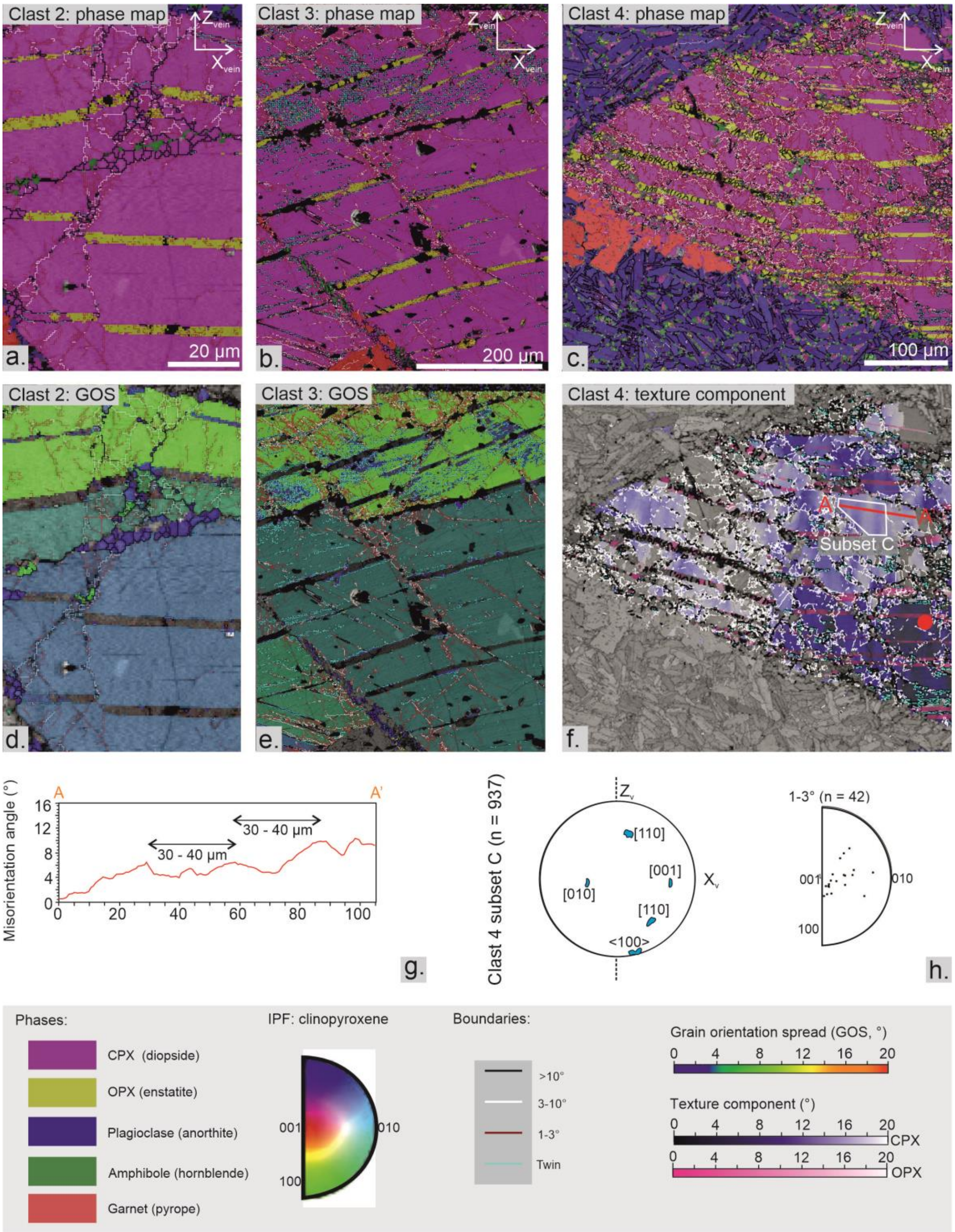

Figure 5. *Microstructures of clinopyroxene clasts 2-4 from EBSD analysis (positions shown in Figs. 2d, f);* ***a)*** *phase map of part of clast 2;* ***b)*** *phase map of part of clast 3;* ***c)*** *phase map of part of clast 4; plus the surrounding pseudotachylyte matrix;* ***d)*** *GOS map of clast 2 (clinopyroxene only) showing increasing values towards the clast edge (top), and very low values in the fine grained crack fill;* ***e)*** *GOS map of clast 3 (clinopyroxene only) showing increasing values towards the clast edge, and very low values in clinopyroxene twins and in fine grained crack fill;* ***f)*** *texture component map for clast 4 showing misorientation relative to the reference point (red dot). clinopyroxene is mapped in blue and orthopyroxene in pink;* ***g)*** *misorientation profiles for A-A' (shown in f.) highlighting regular undulations;* ***h)*** *orientation of axes in clinopyroxene clast 4 (location of subset c shown in f.). The boundary trace parallel to the periodic undulation is indicated by the dashed lines. Rotation axes are displayed in crystal co-ordinates for the same subset.*

Orthopyroxene in the host rock away from the pseudotachylyte veins does not display microstructural evidence of deformation, apart from weak to moderate undulose extinction. In the host rock at the immediate margin of the pseudotachylyte veins N22 and LC1724, orthopyroxene grains are cut by the faults (Figs. 2, 6, 7). These grains show a number of microstructures that are not seen in more distal orthopyroxenes.

In N22, most of the orthopyroxene grain on the margin is fractured (Figs. 6a-b) but a transition is seen from linear fractures (e.g. Fig. 6c) to a particularly fine-grained, pervasively fragmented regions (Figs. 6 d-h). An orthopyroxene grain on the margin of the vein in LC1724 shows a similar feature (Supp. Fig. 3). Within these fragmented regions, there is variation in grain size and shape between subdomains of fine-grained, fairly equant fragments (root-mean-squared grain diameter of 1.4 µm for N22, e.g. Fig. 6f), adjacent regions of coarser grains (Fig. 6e), and regions of larger, more angular fragments locally dissected by intragranular fractures (Figs. 6d, g). The coarser regions (root-mean-squared grain diameter of 2.6 µm for N22) have either equant or rather elongate morphology, with some 120° triple junctions (Figs. 6e, 7b). Both the fine and the coarser (equant and elongate) grains show abundant grain boundary porosity (Figs. 6a-c, 7b).

Elongate grains are seen in several fragmented orthopyroxene grains (Figs. 6e & h, 7, Supp Fig. 3) lying adjacent to the vein margin and have their long axis at a high angle to the vein boundary. Similar elongate fragments occur adjacent to large intragranular cracks within the orthopyroxene host grain (Fig. 6h). Fragmented orthopyroxene occurs also adjacent to non-fractured clinopyroxene, as shown in Supp. Fig. 3c, where orthopyroxene lamellae within clinopyroxene are fragmented next to the vein margin (see Fig. 2 for location of this grain).

The GOS of the fine-grained fragmented orthopyroxene is low relative to the parent orthopyroxene grain (Figs. 7a, Supp Fig. 3d). Low angle boundaries and higher GOS values are, however, seen in some of the coarser fragments. The finer grains show dispersion of orientations away from the crystallographic orientations of the parent orthopyroxene grain but otherwise are generally similar to the parent orientation (Figs. 7b-d, Supp Fig. 3e-f). Misorientation axes are scattered in the fractured grain region (Fig. 8e), although some clustering around [001] is present (Supp Fig. 3f). The more elongate grains have a different CPO to the parent grain, they are preferentially elongate parallel to [001], and show no obvious cluster of misorientation axes (Supp Fig. 3). In general, the fragmented region shows a near- random distribution of misorientation angles between uncorrelated grains but a higher frequency of misorientations <35° between neighbour grains than for a random distribution (Fig. 7f, Supp. Fig. 3h).

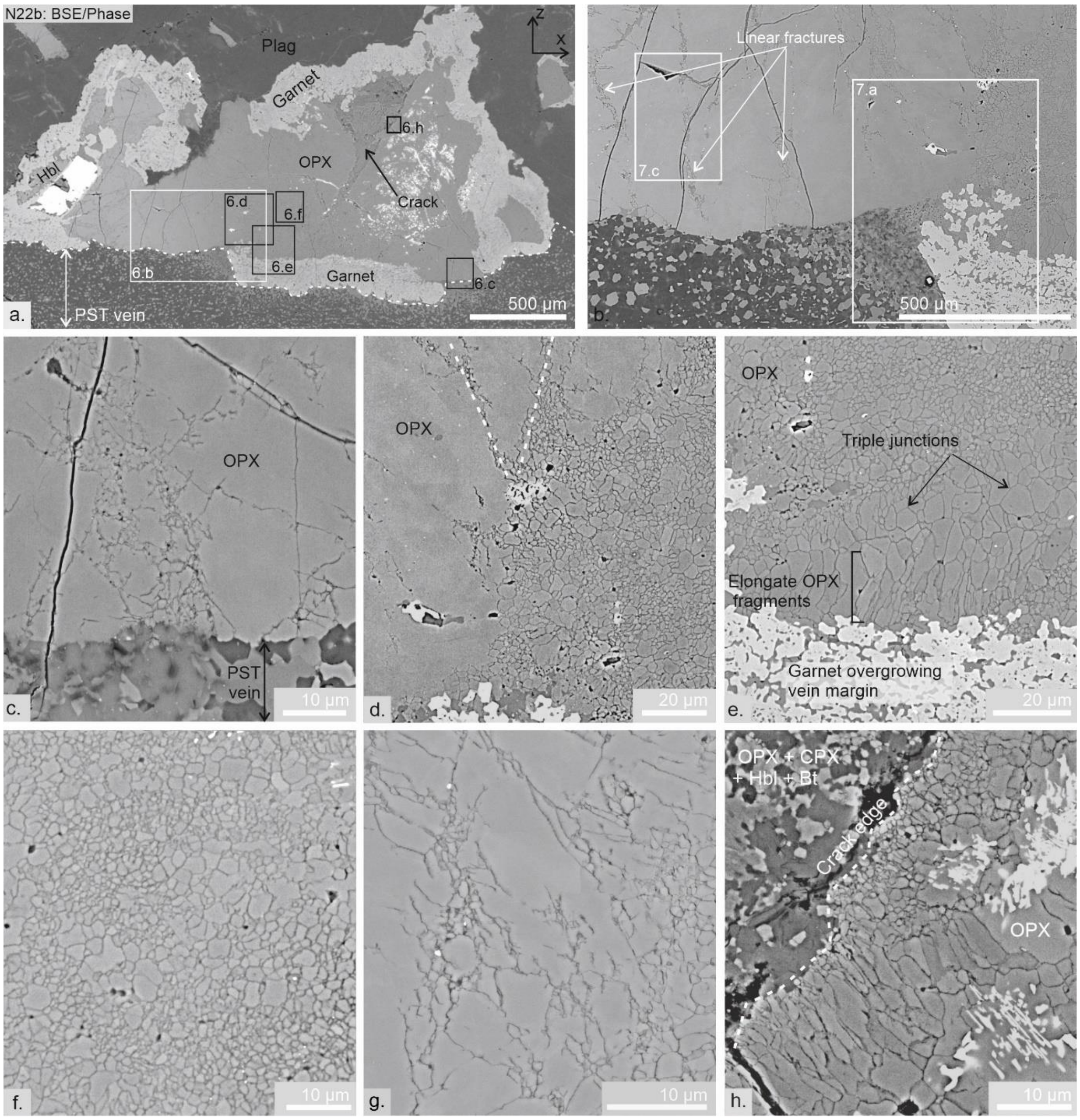

Figure 6. *Backscattered electron (BSE) images of orthopyroxene grain and adjacent pseudotachylyte vein in sample N22:* ***a)*** *View of orthopyroxene grain on margin of pseudotachylyte vein with adjoining phases and subsequent image locations labelled;* ***b)*** *Higher magnification view of same grain illustrating fracture sets across left hand side of grain. Map locations for EBSD analysis shown in Fig. 7 are indicated;* ***c)*** *jigsaw-like fragmentation along cracks;* ***b)*** *edge of pervasively fragmented region. Dashed white lines indicate the main fracture orientations where they meet the fragmented region;* ***c)*** *Variation in fragment size and morphology in pervasively fragmented region;* ***f)*** *high-magnification image of pervasively fragmented region, showing finest grains;* ***g)*** *edge of fragmented region with coarse fragments;* ***h)*** *fragmentation of orthopyroxene around an internal crack filled with biotite plus minor orthopyroxene, clinopyroxene and hornblende.*

The fractures evident in the BSE images of fragmented orthopyroxene (e.g. Figs. 6 b-c,g) correspond to LABs (i.e. with < 10° misorientation across them) or, less frequently, to high-angle boundaries on EBSD maps (Figs. 7a-c). Linear arrays of finer orthopyroxene plus minor clinopyroxene can be seen

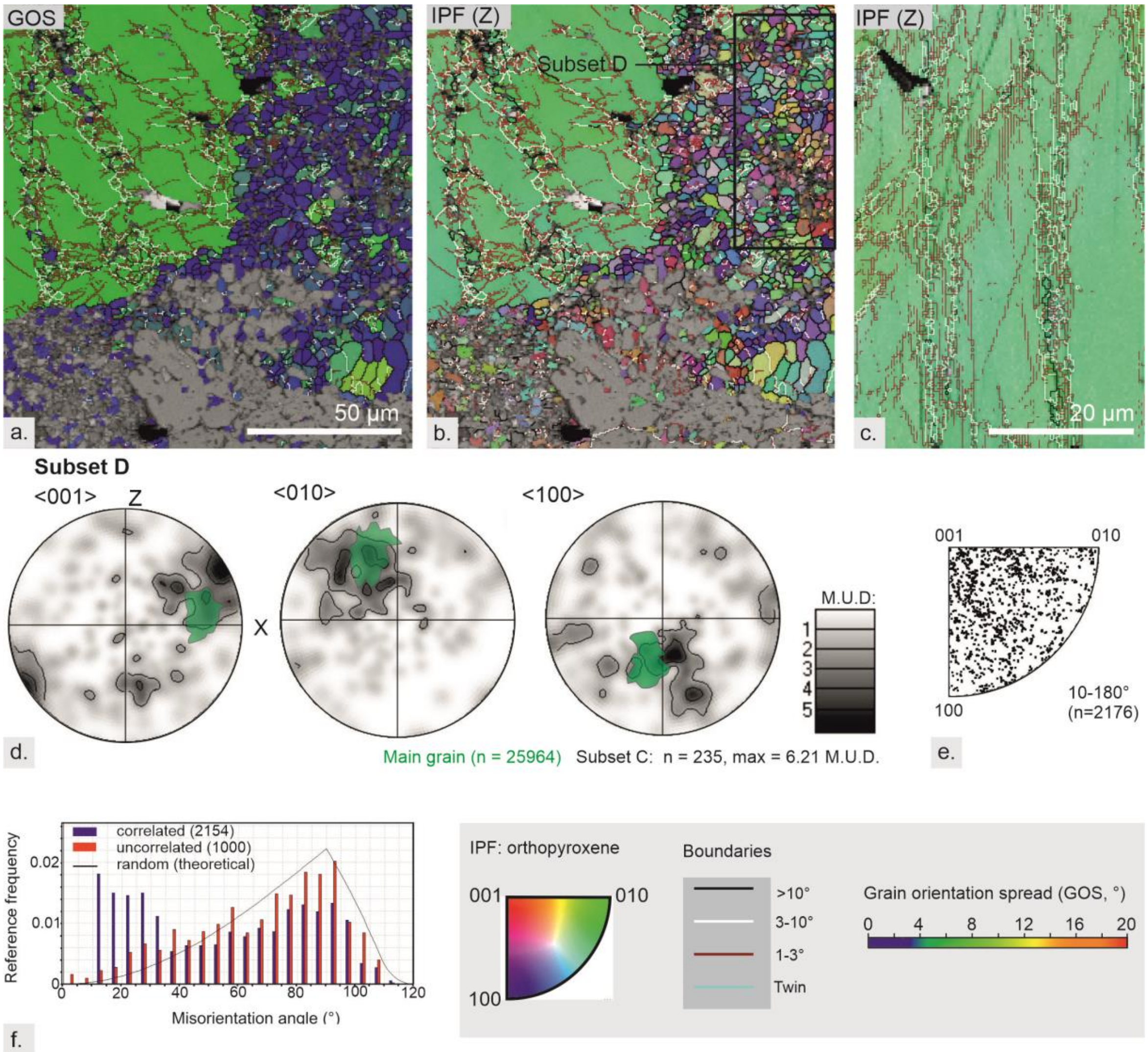

Figure 7. *Microstructures of orthopyroxene in the host rock margin to a pseudotachylyte vein from EBSD analysis (map positions shown in Fig. 6):* ***a)*** *GOS map of edge of fragmented orthopyroxene* ***b)*** *IPF (Z) orientation map of orthopyroxene in same region as a);* ***c)*** *IPX (Z) orientation map of region in centre of orthopyroxene grain* ***d)*** *pole figures for sample of fragmented region – location of this subset D shown b);* ***e)*** ***r****otation axes (in crystal co-ordinates) pole figures for subset D;* ***f)*** *misorientation angle histogram for subset D.*

along the larger of these cracks (Fig. 6b), with coalescence of the finer grained material in fracture intersections (Fig. 6c), but the orientation of the finer-grained orthopyroxene is nearly identical to that of the main grain (Figs. 7 b,c). These linear fractures appear truncated by the zones of more pervasive fracturing (Figs. 6d, 7a-b).

4.3.2 Grain size distribution in the fragmented domains

Some of the regions of fragmented orthopyroxene studied for grain size analysis are shown in Figs. 6 d-g (sample N22) and Supp. Fig. 3a-b (sample LC1724). The sampled set consisted of 2033 grains from N22 and 421 from LC1724. All analysed images were taken from the fragmented regions of the orthopyroxene grains shown in Figs. 6a & 7a. The grain size distribution curve for both samples shows differences between the smaller and larger grain size ranges (Supp. Fig. 4). Both power law and log normal lines of best fit were calculated for sections of the distributions. Using the power law exponent, for N22, the slope of the finer grain size distribution was 2.3 and for the coarser range, 1.2. For LC1724, the finer grained range gave a slope of 1.6, and the coarser range, 3.1 (Supp. Fig. 4) The break in slope is less pronounced in LC1724 but is nevertheless best fit by two separate power law trendlines. In N22 the break of slope is clear and occurs around 4.7 µm.

4.3.3 Clasts in pseudotachylytes

Figure 8 shows the EBSD maps of an orthopyroxene clast in the pseudotachylyte matrix of sample LC1724, consisting of microlitic plagioclase and granular clinopyroxene, hornblende and orthopyroxene (Figs. 1e, 8a). The clast occurs at a distance of 3.4 mm from the margin of the PST vein. Undulose extinction and deformation bands are visible optically (Fig. 1e). EBSD mapping reveals that these bands represent intracrystalline arrays of fine-grained orthopyroxene with very minor interstitial clinopyroxene and hornblende (Fig. 8a). The fine orthopyroxene grains have a maximum GOS of 0.59 (Fig. 8b), a maximum D_{equ} of 6.3 µm and a root-mean squared D_{equ} of 2.1 µm. These arrays dissect the host orthopyroxene clast into domains that have accumulated different amounts of internal deformation, as evident from their different GOS values, overall in the 3-8° range (Fig. 8b).

The orthopyroxene clast shows slight but repeated undulations with parallel orientation (Fig. 8c, Supp. Fig. 1b). These undulations are locally parallel to sharp, linear low-angle boundaries (1-3°) (Fig. 8c). These periodic undulations and the 1-3° low-angle boundaries occur on a semi-regular wavelength of 10-20 µm, giving a crenulated undulose effect (Fig. 8d). The misorientation axis associated with these bands is [001] (Fig. 8e), which is consistent with slip on the (100) [010] system assuming a tilt boundary geometry. The undulations and the low-angle boundaries are cut by the arrays of fine-grained orthopyroxene.

The fine-grained orthopyroxene share a CPO with the host clast, although some dispersion is present (Figs. 8f). The dispersion predominantly occurs around [001]. Polygonal networks of low-angle boundaries, potentially indicating the development of subgrains, have not been observed in the clast.

5. Discussion

5.1 Overprinting relationships between deformation microstructures

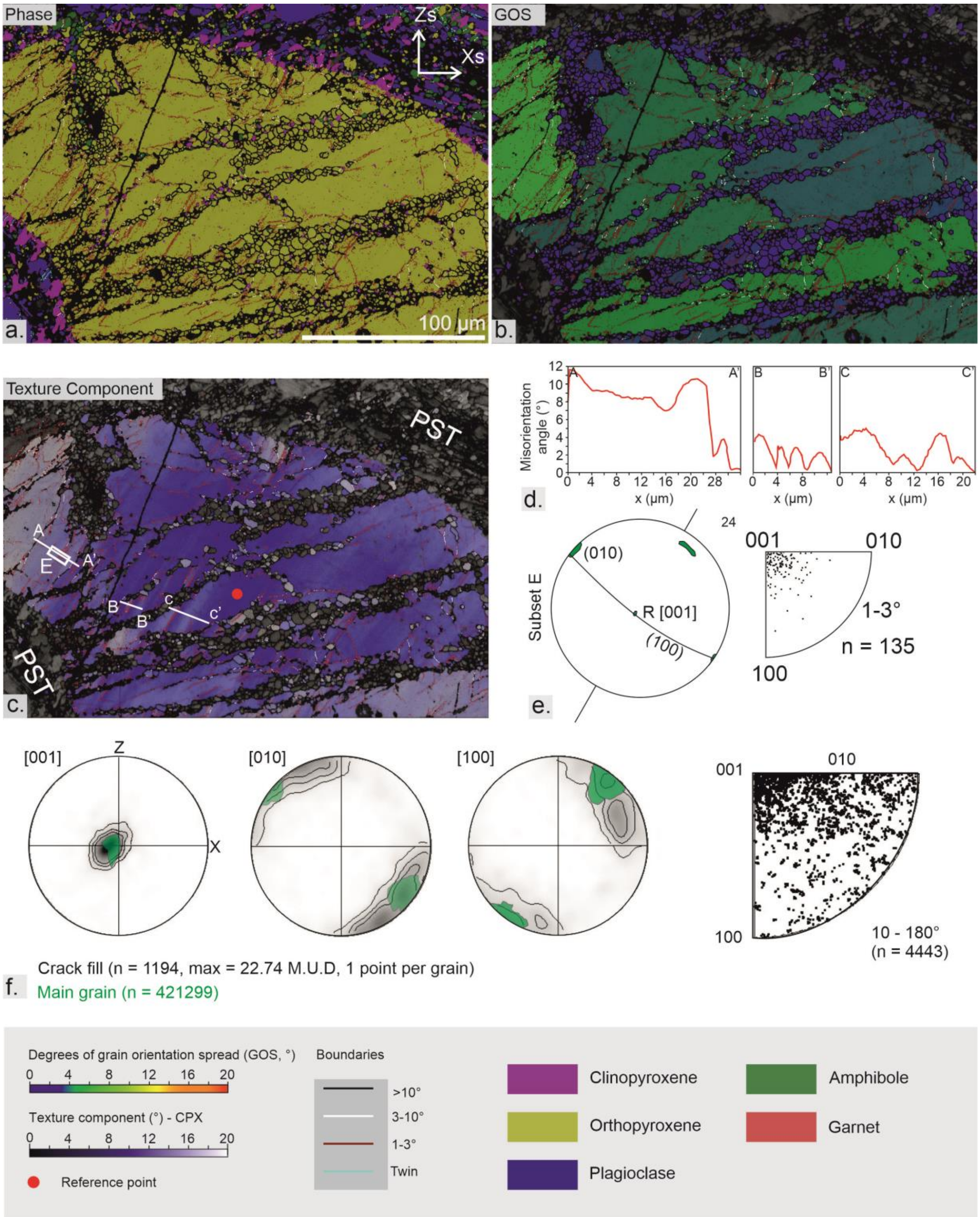

Figure 8. *Microstructures of orthopyroxene clast from EBSD analysis;* ***a)*** *Phase map of analysed region of clast and surrounding pseudotachylyte matrix;* ***b)*** *GOS map of orthopyroxene. Fine-grained arrays of orthopyroxene have low GOS values (blue colouring);* ***c)*** *Texture component map of orthopyroxene, red dot locates reference point;* ***d)*** *misorientation profiles along A-A' B-B' and C-C', indicated in c);* ***e)*** *pole figure and low-angle rotation axes (in crystal co-ordinates) for subset D, location shown in c);* ***f)*** *pole figures and high-angle rotation axes for the fine-grained orthopyroxene arrays within the clast. Green overlay shows distribution of points from the main grain.*

Deformation twins occurs pervasively in clinopyroxene, both in clasts in the pseudotachylyte veins as well as in host rock grains situated at least up to 8 mm away from the vein margin (Fig. 3b).

Deformation twinning predominantly developed on (001), although additional (100) twins are developed in clast 3 (Fig. 5b) where the clustering of (100) twins near the clast boundary implies that additional (100) twinning may have been driven by deformation conditions along the fault. However, twin boundaries are generally bent and cut by LABs, by cracks, and by periodic low (1-3°) misorientation bands (Figs. 4, 5), implying that twinning is typically the earliest microstructural record of deformation in clinopyroxene, and extends some distance into the wall-rock.

Other deformation microstructures are limited to clasts within the pseudotachylyte fault zone, suggesting that they relate to highly localised deformation associated with the seismic rupture. These are the periodic undulations with 20-40 µm wavelength, which overprint orthopyroxene exsolution lamellae (Fig. 5f) and deformation twins, but are cut and offset by linear LABs (Fig. 4). The LABs are cut by the final stage of deformation in the clinopyroxene clasts, fracturing and grain growth in intracrystalline bands of fine-grained clinopyroxene ± amphibole ± garnet (Fig. 5a,b).

In orthopyroxene, fracturing and fragmentation is preserved in grains in the wall rock margin as well as in survivor clasts. In the wall-rock margin, the dominant microstructure is fracturing (Figs. 6b-c) and local regions of pervasive fragmentation (Figs. 6-7, Supp. Fig. 3). In the orthopyroxene clast analysed with EBSD, undulating misorientation resulting from glide on (100)[010] is cut by intracrystalline bands of fine-grained orthopyroxene ± clinopyroxene ± amphibole (Fig. 8). Because other orthopyroxene clasts show pervasive fragmentation similar to the margin grains (Supp. Fig. 3,5), we suggest that the analysed orthopyroxene clast in Fig. 8 preserves the earlier signature of dislocation glide, which has escaped fragmentation.

In summary, we interpret these overprinting relationships to reflect the pre- to co-seismic deformation of pyroxene in response to local stress amplifications that triggered the generation of type-2 pseudotachylytes in Nusfjord. In the following sections, we propose a conceptual model for the association of these stress changes with the seismic cycle already partly recorded by the presence of pseudotachylyte.

5.2 High stress loading: deformation by low-temperature plasticity

Twinning via (100)[001] in clinopyroxene occurs at a critically resolved shear stress of 100-140 MPa but is not dependent on temperature or strain rate (Kollé & Blacic, 1982). The presence of twinning in host rock clinopyroxene grains away from the vein margin suggests that this early stage of deformation was driven by stresses that were not entirely localised to the fault plane. This may be related to the earliest heterogeneous stress amplifications that built up prior to failure, less localised to the eventual rupture zone than the later microstructures in clasts that all cross-cut twinning.

Most clinopyroxene clasts illustrated here show deformation by low-temperature plasticity controlled by dislocation glide along (100)[001], producing LABs and undulating misorientation that cut the twin boundaries and the orthopyroxene exsolution lamellae. (100)[001] is the typical glide system in clinopyroxene (Avé Lallemant, 1978; Ingrin et al., 1992; Kirby & Kronenberg, 1984; Kollé & Blacic, 1983; Raleigh & Talbot, 1967). In our samples, evidence of any transition to dislocation creep is absent, consistent with the relatively low temperature conditions of deformation for crystal plasticity in clinopyroxene (e.g. Bystricky & Mackwell 2001). Flow laws extrapolated to natural strain rates for dislocation glide of diopside require several 100 MPa or GPa of differential stress for Peierls-controlled glide to occur in clinopyroxene (Fig. 9). Results from the micro-indentation tests of Dorner & Stöckhert (2004) suggest that, at relatively low strain rates of 10^{-14} s^{-1} and a temperature range of 600-700°C, between 1.6-2.0 GPa would be needed to activate Peierls-controlled glide. If strain rates were to increase towards seismic strain rates, for example a rapid strain rate of 10^{-3} s^{-1}, the required flow stress increases to 3.7-3.9 GPa (Fig. 9). Based on the flow law for Peierls-controlled glide of Kollé & Blacic (1983), at temperatures of 600-700°C strain rates > 10^{-12} s^{-1} are necessary to induce glide, and at strain rates of 10^{-9} s^{-1} or greater, critical resolved shear stresses would be > 1 GPa (at 700°C) and > 3 GPa (at 600°C) (Fig. 9). This glide law was observed by Kollé & Blacic (1983) to initiate at critically resolved shear stresses > 520 MPa in hedenbergite crystals poorly orientated for twinning; in crystals where twinning was possible, dislocation glide required temperatures > 850 °C under their experimental conditions. Without knowing the stress orientation, it is not possible to convert an equivalent differential stress, but the differential stress must be at least twice the resolved shear stress. We therefore infer that the low-temperature plasticity microstructures observed in clinopyroxene clasts occurred as a response to transient and localised differential stresses in excess of 1 GPa. The localisation of these microstructures to the clasts, and not in the clinopyroxene grains which now form the margin to the pseudotachylyte vein, suggests that these high stresses were localised to the rock volume that subsequently formed the pseudotachylyte fault vein. However, overprinting by fracturing indicates that this localisation occurred prior to passage of the rupture tip.

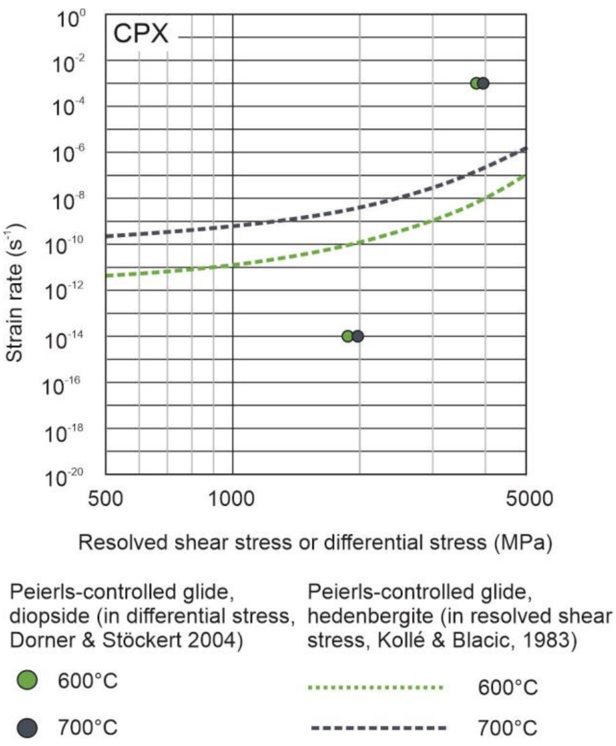

Figure 9. *Two flow laws for Peierls-controlled glide in diopside (Dorner & Stöckert, 2004) and hedenbergite (Kollé & Blacic, 1983) at temperatures for deformation in Nusfjord (600-700°C). The law from Dorner & Stöckert (2004) is shown at strain rates of 10^{-14} s^{-1} (i.e. a background geological strain rate) and at a very rapid 10^{-3} s^{-1} (for approximation of acceleration towards seismic slip rates). The law from Kollé & Blacic (1983) is for Peierls glide on (100) [001] for < 900°C and > 520 MPa. Note that the x-axis shows differential stress for Dorner & Stöckert (2004) but resolved shear stress for the laws of Kollé & Blacic (1983).*

The regular 20-40 µm wavelength periodic undulation of the clinopyroxene lattice (Figs. 4f, 5g) bears some similarities to the short-wavelength undulatory extinction (SWUE) recognised in quartz (Trepmann & Stöckhert, 2013) and olivine (Druiventak *et al., 2012)* ‘kick-and-cook’ experiments, although the undulation in clinopyroxene has a longer wavelength. The undulose misorientation is characterised purely by continuous sinusoidal curvature of the crystal lattice, which was accommodated by glide along the (100)[001]. Similar periodic undulations occur also in orthopyroxene clasts (Fig. 8d) and are consistent with dislocation glide on (100)[010] (Fig. 8e).

The formation of SWUE in quartz was attributed to high stress dislocation glide (‘kick’-phase) that generates lamellae of tangled dislocations (Trepmann & Stöckhert, 2013). Natural comparisons to SWUEs have been proposed in quartz (Brückner & Trepmann, 2021, Birtel & Stöckhert, 2008, Trepmann & Seybold, 2019) and olivine (Matysiak & Trepmann, 2012) but not, to our knowledge, previously in pyroxenes. The generation model for SWUEs of Trepmann & Stöckhert (2013), invoking dislocation glide under high stresses caused by seismic loading, is inviting because of the shared deformation mechanism (glide) observed in these pyroxenes, and because of the seismic context of the Nusfjord samples. The parallels are especially clear in the recent work of Brückner & Trepmann, (2021) who observe SWUEs in quartz adjacent to pseudotachylytes. We propose that the periodic undulations in clinopyroxene were produced by a low-temperature plasticity response to the highest stresses localised around the eventual fault plane. After twinning, the periodic undulations are the next earliest microstructure to form in clinopyroxene, and in orthopyroxene are cut by fractures. Hence they are potentially related to the stress concentrations during loading, preceding eventual rupture.

SWUEs in quartz and olivine were attributed to high-stress loading of the mid- to lower-crust via shallower earthquake activity (Birtel & Stöckhert, 2008; Malysiak & Trepmann, 2012; Trepmann & Stöckhert 2013). The context of the seismic environment in Nusfjord, where type-2 pseudotachylytes represent the in-situ nucleation of short earthquake ruptures (Campbell et al. 2020), fits better with the observations of Brückner and Trepmann (2021) that such glide-controlled microstructures also occur adjacent to in situ seismic rupture within the mid- to lower- crust. Our evidence supports transient high stress loading either being a result of local stress amplifications preceding and eventually causing rupture nucleation (Campbell et al., 2020), or as a response to high rupture tip stresses (Reches & Dewers, 2005). The former is prefered due to the overprinting of glide structures in orthopyroxene by later fragmentation that can be linked with more confidence to dynamic rupture tip processes.

5.3 Coseismic deformation: pulverisation of orthopyroxene

The fine-grained orthopyroxene at the pseudotachylyte fault vein margin (Figs. 6-8) is interpreted to have formed via brittle grain size reduction, based on: a) the fracture systems evident in BSE micrographs (Fig. 6) and the jigsaw-breccia type grain shapes preserved in some fine-grained regions (Fig. 6g), and b) the absence of polygonal subgrains from the interior of the large orthopyroxene fragments, in accordance with the expected lack of recovery in orthopyroxene at the deformation temperature of 700-750 °C (e.g. Kohlstedt & Vander Sande, 1973; Kanagawa et al., 2008). The lack of shear between large fragments (Figs. 6,7) supports that pulverisation, rather than cataclasis, was the main fragmentation process in orthopyroxene. The lack of shear is also evident in the overlap in crystallographic orientation between the fine grains and the coarser fragments (Fig. 7d, see also

Petley-Ragan at al., 2019 and Soda & Okudaira, 2018). An alternative explanation of thermal shock was ruled out due to the lack of fracturing in the orthopyroxene clast (Fig. 8), which, being within the vein, should have experienced higher coseismic temperatures than the wall rock (Papa et al., 2018), although other orthopyroxene clasts do show pervasive fragmentation (Supp. Fig. 5).

Although pulverisation is considered to be depth-limited by increasing confining pressure (Aben et al., 2017; Yuan et al., 2011), pervasive damage zones extending up to 200 m from the fault have been exhumed from crustal depths below the frictional viscous transition (Sullivan & Peterman, 2017). Interpretations of pulverisation of single grains have recently accumulated from microstructural studies of lower crustal seismicity in both naturally and experimentally deformed rocks (Austrheim et al., 2017; Soda and Okudaira, 2018; Incel *et al.*, 2019; Petley-Ragan *et al.*, 2019; Song *et al.*, 2020). Minerals observed to undergo pulverisation-style fragmentation include plagioclase (Soda & Okudaira, 2018), garnet (Austrheim et al., 2017; Incel et al., 2019; Petley-Ragan et al., 2019; Song et al., 2020) and diopside (Petley-Ragan et al., 2019). In the Nusfjord samples, orthopyroxene is the only mineral to show microstructures compatible with pulverisation-style fragmentation.

Pulverisation-style fragmentation, particularly where tensile fracturing is involved, is attributed to dynamic rupture tip stress fields that overcome the high confining pressure (Reches & Dewers, 2005), but has also been linked to the passage of seismic shockwaves ahead of the rupture front (Doan & Gary, 2009) and by impulsive coseismic loading and unloading of the wall-rocks (Brune, 2001). The asymmetry of fragmentation observed in the field along major tectonic faults favours a link with the asymmetric rupture tip stress fields, where one side of the tip is in compression and the other in tension (Dor et al., 2006; Petley-Ragan et al., 2019; Reches & Dewers, 2005; Wilson et al., 2005; Xu & Ben-Zion, 2017). Although supershear ruptures may favour pulverisation (Yuan et al., 2011), sub-shear ruptures should also induce extreme stress and strain rate conditions a few mm from the rupture – one calculation predicts 5 GPa tensional stress and ~10^5 s^{-1} dilation in this zone (Wilson et al., 2005). In our samples, it is not easy to judge whether the pulverisation occurs on one side of the fault only, because there is no orthopyroxene visible in the opposing wall to compare with. Whilst fragmented orthopyroxene occurs within clasts in the vein, the delocalisation effect of the pseudotachylyte melt makes it impossible to know where the initial rupture plane was in relation to the in situ position of that grain. There is evidence for injection veins and damage on both sides of the fault in one sample (Fig 2c-d), which may dispute asymmetry (although injection veins are not always linked to rupture-tip stress fields) – however, the alternative models of impulsive loading cycles or shockwaves (Brune, 2001, Doan & Gary, 2009) are also coseismic processes and do not change our interpretation of the timing of these microstructures.

5.4 Grain growth of orthopyroxene driven by short-term heat pulse

Many of the orthopyroxene fragmented grains are somewhat modified in shape. Grain growth from the fine-grained fragments is apparent in the elongate orthopyroxene grains, as well as in regions with well-developed 120° triple junctions (Fig. 6e). Grain-size distributions (Supp. Fig. 4) are commonly used to determine processes of fracturing, faulting, and grain growth (e.g. Sammis *et al.* 1986), although the various mechanisms of brittle fragmentation are not always easily distinguishable via this analysis (Stünitz et al., 2010; Wilson et al., 2005). The observed range of 2D slope values in our analysis, 1.2-3.1 (Supp. Fig. 4), is comparable with grain size distributions reported for mid- to lower-crustal seismic deformation (Aupart et al., 2018 and references therein; Jamtveit et al., 2019; Soda and Okudiara, 2018; Song et al., 2020) including those attributed to coseismic pulverisation of garnet, olivine and plagioclase. Neither of our samples are conducive to a single best-fit power law or log normal distribution, with the break in slope estimated at a diameter

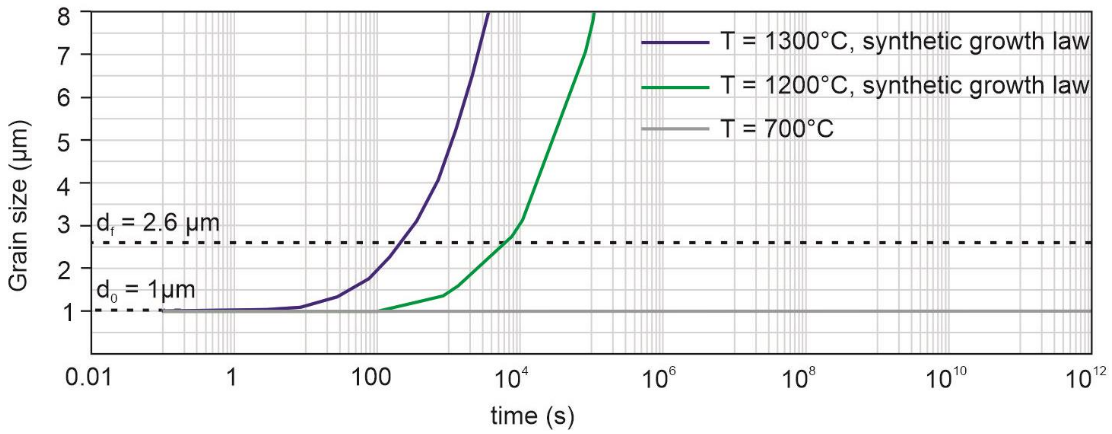

Figure 10. *OPX grain growth modelling from initial diameter of 1 µm. Growth law parameters from the synthetic samples of Skemer & Karato (2007) are used to compare rates for 1300 °C and 1200 °C; for 700 °C, the rate constant k (rate constant) is extrapolated from enthalpy and k_0 values provided in the same publication*

of around 4.7 µm for both samples. We suggest that this change in slope reflects modification of the original fragmentation grain size by the subsequent grain growth apparent in the BSE images. This is consistent with the findings of Keulen et al. (2007) and Aupart et al., (2018) that changes in GSD slope reflect a switch in grain processes.

The CPO of the elongate grains differs to that of the more equant fragments, which tend to be similar to the parent CPO (Supp. Fig. 3f-g). The short axes of the elongate grains are of a similar size to the diameter of the equant grains, suggesting that the elongate grains may have formed via a mix of rotation and growth of existing fragments. The shape preferred orientation is always at a high angle to the vein edge (Figs 6-7, Supp. Fig. 3) and the grain elongation is predominantly parallel to [001], which has been reported as the fastest diffusion and growth direction in orthopyroxene (Milke et al., 2013; Dohmen et al., 2016). This elongation is also observed at the edge of a large intracrystalline tensile crack within a host rock margin orthopyroxene grain (Figs. 6a,h) which extends between points of 0.34 - 1.09 mm perpendicular distance from the pseudotachylyte vein edge. The apparent orientation of the crack forms a high angle to the fault vein, suggesting that the crack was tensile, as does the parallel elongation of the orthopyroxene, perpendicular to the crack. This geometry is similar to tensile cracks formed within dynamic stress fields linked to crack tip propagation (Ngo et al., 2012), suggesting that it may have formed concurrent with the pulverisation-style fragmentation within the grain. The distribution of the elongate grains along the edge of this crack as well as along the pseudotachylyte vein margin therefore implies that elongate grain growth occurred after fragmentation but potentially concurrent with continued slip and the associated frictionally generated thermal pulse that drove melting along the fault plane.

Because of the transience of frictional heating, grain growth needs to take place during, or immediately after, seismic slip. Using the orthopyroxene grain growth laws of Skemer & Karato (2007), we assess the potential growth time necessary for a starting orthopyroxene fragment size of 1.0 µm at temperatures ranging from 1300 °C - close to typical pseudotachylyte maximum melt temperatures (Sibson & Toy, 2006) - down to an ambient temperature of 700 °C (Fig 10.). At 700 °C, the orthopyroxene will not achieve the required grain size of D_{equ} = 2.6 µm (for the elongate grains) within 3 Ga, implying that some form of heat pulse must be required for grain growth. At temperatures around 1300°C the required grain growth may be achieved within 16 minutes and at 1200 °C, within 3 hours (Fig. 10). These temperatures can be feasibly generated during coseismic frictional heating, so that growth of the elongate grains may have initiated during slip.

5.5 Conceptual model of pre-and co-seismic deformation in pyroxenes

Based on the overprinting relationships of microstructures in the pyroxenes (sections 4.2-4.3) and our interpretations of their deformation mechanisms plus resulting stress and temperature implications, we suggest a conceptual model of pre- and co-seismic deformation of clino- and orthopyroxene (Fig. 12).

1. Distributed twinning seen in clinopyroxene appears to be spatially associated with pseudotachylyte veins but are not as localised as subsequent deformation microstructures. The critical shear stresses associated with clinopyroxene twinning (Kollé & Blacic, 1982) are not especially high relative to expected failure strength; twinning may relate to progressive stress amplification prior to the failure stress being reached (Campbell et al., 2020).

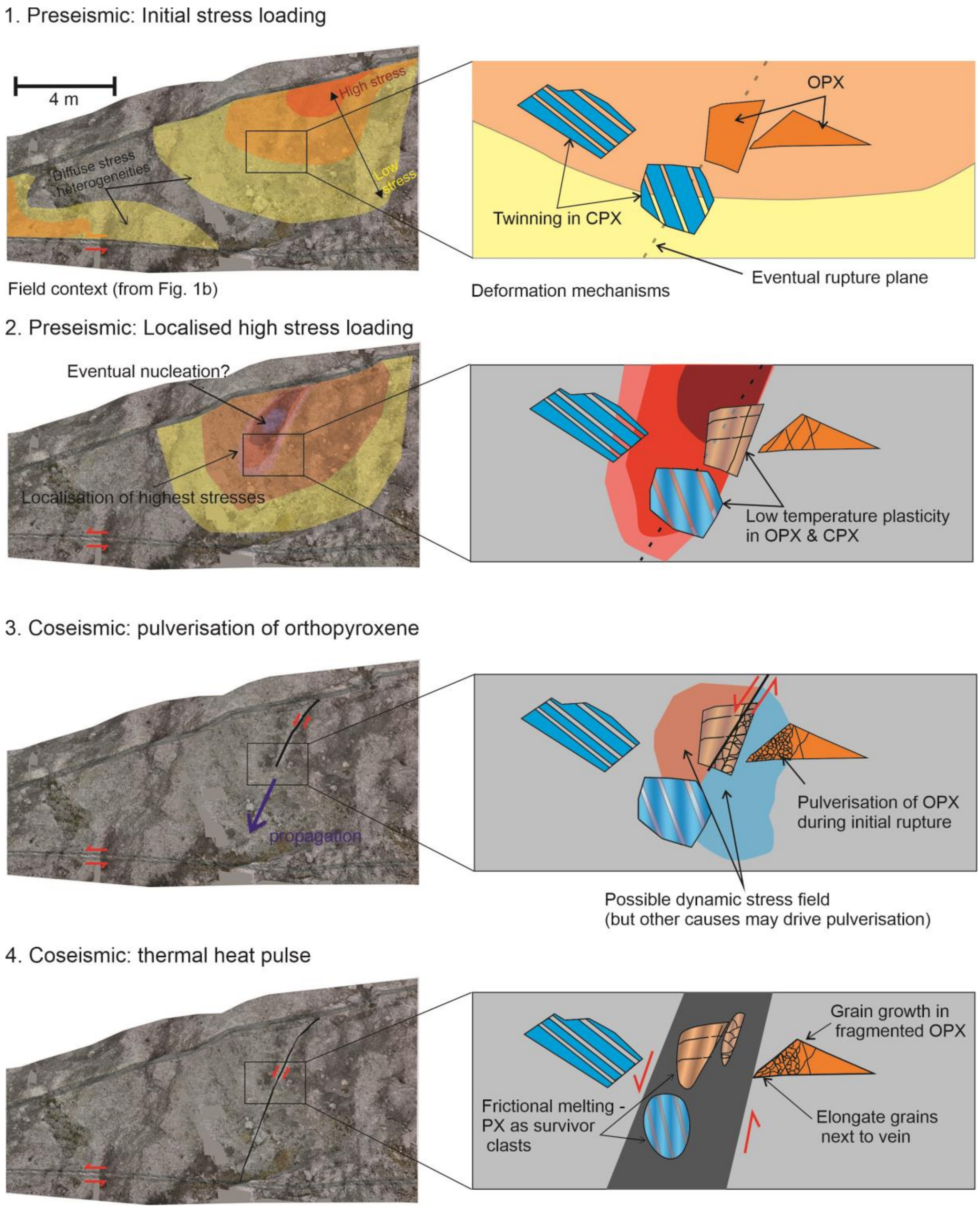

Figure 11. *Proposed order and association of pyroxene microstructure with potential rupture processes. A conceptual example from the context of the shear-zone bounded block shown in Fig. 1b – in this example, the pre-seismic stress loading is thought to be driven by the activity of the shear zones (Campbell et al., 2020).*

2. Low temperature plasticity in clinopyroxene and orthopyroxene is predominantly found within clasts, suggesting much more pronounced localisation of stress (potentially > 1 GPa, Fig. 12) around the eventual rupture plane. This is consistent with interpretations made for similar high-stress dislocation glide-controlled microstructures observed in both naturally and experimentally deformed rocks (Druiventak *et al.* 2011; Matysiak & Trepmann 2012; Trepmann *et al.* 2013).
3. Low temperature plasticity is overprinted by pulverisation-style fragmentation in orthopyroxene, which most likely relates to dynamic stress fields related to the passage of the rupture tip (the 'fault tip process zone' of Petley-Ragan et al., 2018 – their Fig. 4), or alternatively may relate to impulsive loading or shockwaves. There appears to be no microstructural record for this stage in the clinopyroxene.
4. After the passage of the rupture tip, frictional heating during continued seismic slip melts phases along the fault plane, eventually cooling to form the pseudotachylyte vein. Fragments of pyroxene and plagioclase, sourced from the fault walls and comminuted material, may survive, unmelted, as clasts. Conduction of the frictional heat pulse into the wall rock is a feasible driver of (oriented) grain growth within the fragmented orthopyroxene immediately adjacent to the pseudotachylyte vein.

5. Conclusions

Deformation mechanisms in both clino- and orthopyroxenes spatially associated with ancient seismogenic faults from Nusfjord (Lofoten, Norway) record increasing localisation of progressively higher stress (up to GPa in magnitude) prior to rupture, preceding pulverisation-style fragmentation of orthopyroxene potentially linked to the passage of the rupture tip. The spatial association of these microstructures with a single-slip pseudotachylyte-bearing fault plane, constrained to represent seismic rupture nucleating at lower crustal depths of 25-30 km, implies that the sequence of overprinting microstructures may be linked to increasing loading and eventual rupture during one lower crustal seismic cycle.

The extent to which low-temperature plasticity within lower crustal granulites can accommodate transient stress amplifications may be an important control on when and where rupture and subsequent seismic damage can initiate with the lower crust. Intracrystalline deformation of phases along the fault plane and in the damage zone is an increasingly recognised and valuable record of the short-term changes to the stress regime prior to rupture in lower crustal rocks.

Acknowledgements

This work was supported by the UK Natural Environment Research Council (grant NE/P001548/1 "The Geological Record of the Earthquake Cycle in the Lower Crust"). We thank colleagues at the Plymouth Electron Microscopy Centre for guidance and support with SEM analysis. Sample N22 was collected by Elliot Wood and Katherine Harris during their MGeol project at the University of Plymouth. Unfortunately Elliot is no longer with us to see the completion of this work. This paper is dedicated to him, and to his passion for science and nature.

Open Research

Available data in support of this work include: unfiltered EBSD datasets, images used for grains size data analysis, spreadsheets showing calculations for grain size data analysis and grain growth modelling. These data are available at the British Geological National Geoscience Data Centre via https://webapps.bgs.ac.uk/services/ngdc/accessions/index.html#item169329 under a non-exclusive in-perpetuity licence.

Aben, F. M., Doan, M.-L., Gratier, J.-P., & Renard, F. (2017, June 30). Coseismic Damage Generation and Pulverization in Fault Zones. *Fault Zone Dynamic Processes*. https://doi.org/doi:10.1002/9781119156895.ch4

Anderson, E. K., Song, W. J., Johnson, S. E., & Cruz-Uribe, A. M. (2021). Mica kink-band geometry as an indicator of coseismic dynamic loading. *Earth and Planetary Science Letters*, *567*, 117000. https://doi.org/https://doi.org/10.1016/j.epsl.2021.117000

Aupart, C., Dunkel, K. G., Angheluta, L., Austrheim, H., Ildefonse, B., Malthe-Sørenssen, A., & Jamtveit, B. (2018). Olivine Grain Size Distributions in Faults and Shear Zones: Evidence for Nonsteady State Deformation. *Journal of Geophysical Research: Solid Earth*, *123*(9), 7421–7443. https://doi.org/10.1029/2018JB015836

Austrheim, H., Dunkel, K. G., Plümper, O., Ildefonse, B., Liu, Y., & Jamtveit, B. (2017). Fragmentation of wall rock garnets during deep crustal earthquakes. *Science Advances*, *3*(2). Retrieved from http://advances.sciencemag.org/content/3/2/e1602067.abstract

Avé Lallemant, H. G. (1978). Experimental deformation of diopside and websterite. *Tectonophysics*, *48*(1), 1–27. https://doi.org/https://doi.org/10.1016/0040-1951(78)90083-5

Bestmann, M, Pennacchioni, G., Nielsen, S., Göken, M., & de Wall, H. (2012). Deformation and ultrafine dynamic recrystallization of quartz in pseudotachylyte-bearing brittle faults: A matter of a few seconds. *Journal of Structural Geology*, *38*(0), 21–38. https://doi.org/10.1016/j.jsg.2011.10.001

Birtel, S., & Stöckhert, B. (2008). Quartz veins record earthquake-related brittle failure and short term ductile flow in the deep crust. *Tectonophysics*, *457*(1–2), 53–63. https://doi.org/http://dx.doi.org/10.1016/j.tecto.2008.05.018

Brückner, L. M., & Trepmann, C. A. (2021). Stresses during pseudotachylyte formation - Evidence from deformed amphibole and quartz in fault rocks from the Silvretta basal thrust (Austria). *Tectonophysics*, *817*, 229046. https://doi.org/https://doi.org/10.1016/j.tecto.2021.229046

Brune, J. N. (2001). Fault-normal dynamic unloading and loading: An explanation for" non-gouge" rock powder and lack of fault-parallel shear bands along the San Andreas Fault. In *AGU Fall Meeting Abstracts*. San Francisco: AGU.

Bystricky, M., & Mackwell, S. (2001). Creep of dry clinopyroxene aggregates. *Journal of Geophysical Research: Solid Earth*, *106*(B7), 13443–13454. https://doi.org/10.1029/2001JB000333

Campbell, L. R., & Menegon, L. (2019). Transient High Strain Rate During Localized Viscous Creep in the Dry Lower Continental Crust (Lofoten, Norway). *Journal of Geophysical Research: Solid Earth*, *124*, 10240–10260. https://doi.org/10.1029/2019JB018052

Campbell, L. R., Menegon, L., Fagereng, & Pennacchioni, G. (2020). Earthquake nucleation in the lower crust by local stress amplification. *Nature Communications*, *11*(1), 1322. https://doi.org/10.1038/s41467-020-15150-x

Campbell, L., Menegon, L. (2021). Electron backscatter diffraction data and sample analysis from the Nusfjord Shear Zone, Lofoten, Norway. NERC EDS National Geoscience Data Centre. (Dataset). https://doi.org/10.5285/fc332502-1b15-48db-a4f0-16274e924ba0

Corfu, F. (2004). U–Pb Age, Setting and Tectonic Significance of the Anorthosite–Mangerite–Charnockite–Granite Suite, Lofoten–Vesterålen, Norway. *Journal of Petrology*, *45*(9), 1799–1819. Retrieved from http://dx.doi.org/10.1093/petrology/egh034

Doan, M.-L., & Gary, G. (2009). Rock pulverization at high strain rate near the San Andreas fault. *Nature Geoscience*, *2*(10), 709–712. https://doi.org/10.1038/ngeo640

Dohmen, R., Ter heege, J. H., Becker, H.-W., & Chakraborty, S. (2016). Fe-Mg interdiffusion in orthopyroxene. *American Mineralogist*, *101*(10), 2210–2221. https://doi.org/10.2138/am-2016-5815

Dor, O., Rockwell, T. K., & Ben-Zion, Y. (2006). Geological Observations of Damage Asymmetry in the Structure of the San Jacinto, San Andreas and Punchbowl Faults in Southern California: A Possible Indicator for Preferred Rupture Propagation Direction. *Pure and Applied Geophysics*, *163*(2), 301–349. https://doi.org/10.1007/s00024-005-0023-9

Dorner, D., & Stöckhert, B. (2004). Plastic flow strength of jadeite and diopside investigated by microindentation hardness tests. *Tectonophysics*, *379*(1), 227–238. https://doi.org/https://doi.org/10.1016/j.tecto.2003.11.008

Druiventak, A., Trepmann, C. A., Renner, J., & Hanke, K. (2011). Low-temperature plasticity of olivine during high stress deformation of peridotite at lithospheric conditions — An experimental study. *Earth and Planetary Science Letters*, *311*(3), 199–211. https://doi.org/https://doi.org/10.1016/j.epsl.2011.09.022

Druiventak, A., Matysiak, A., Renner, J., & Trepmann, C. A. (2012). Kick-and-cook experiments on peridotite: simulating coseismic deformation and post-seismic creep. *Terra Nova*, *24*(1), 62–69.

https://doi.org/10.1111/j.1365-3121.2011.01038.x

Dunkel, K. G., Zhong, X., Arnestad, P. F., Valen, L. V., & Jamtveit, B. (2020). High transient stress in the lower crust: Evidence from dry pseudotachylytes in granulites, Lofoten Archipelago, northern Norway. *Geology*, *49*(2), 135–139. https://doi.org/10.1130/G48002.1

Ellis, S., & Stöckhert, B. (2004). Imposed strain localization in the lower crust on seismic timescales. *Earth, Planets and Space*, *56*(12), 1103–1109. https://doi.org/10.1186/BF03353329

Ferrand, T. P., Hilairet, N., Incel, S., Deldicque, D., Labrousse, L., Gasc, J., et al. (2017). Dehydration-driven stress transfer triggers intermediate-depth earthquakes. *Nature Communications*, *8*, 15247. Retrieved from http://dx.doi.org/10.1038/ncomms15247

Hacker, B. R., Peacock, S. M., Abers, G. A., & Holloway, S. D. (2003). Subduction factory 2. Are intermediate-depth earthquakes in subducting slabs linked to metamorphic dehydration reactions? *Journal of Geophysical Research: Solid Earth*, *108*(B1), 2030. https://doi.org/10.1029/2001JB001129

Hawemann, F., Mancktelow, N. S., Pennacchioni, G., Wex, S., & Camacho, A. (2019). Weak and Slow, Strong and Fast: How Shear Zones Evolve in a Dry Continental Crust (Musgrave Ranges, Central Australia). *Journal of Geophysical Research: Solid Earth*, *124*(1), 219–240. https://doi.org/10.1029/2018JB016559

Incel, S., Schubnel, A., Renner, J., John, T., Labrousse, L., Hilairet, N., et al. (2019). Experimental evidence for wall-rock pulverization during dynamic rupture at ultra-high pressure conditions. *Earth and Planetary Science Letters*, *528*, 115832. https://doi.org/https://doi.org/10.1016/j.epsl.2019.115832

Ingrin, J., Doukhan, N., & Doukhan, J.-C. (1992). Dislocation glide systems in diopside single crystals deformed at 800-900°C. *European Journal of Mineralogy*, *4*(6), 1291–1302. https://doi.org/10.1127/ejm/4/6/1291

Jamtveit, B., Ben-Zion, Y., Renard, F., & Austrheim, H. (2018). Earthquake-induced transformation of the lower crust. *Nature*, *556*(7702), 487–491. https://doi.org/10.1038/s41586-018-0045-y

Jamtveit, B., Petley-Ragan, A., Incel, S., Dunkel, K. G., Aupart, C., Austrheim, H., et al. (2019). The Effects of Earthquakes and Fluids on the Metamorphism of the Lower Continental Crust. *Journal of Geophysical Research: Solid Earth*, *0*(0). https://doi.org/10.1029/2018JB016461

Kanagawa, K., Shimano, H., & Hiroi, Y. (2008). Mylonitic deformation of gabbro in the lower crust: A case study from the Pankenushi gabbro in the Hidaka metamorphic belt of central Hokkaido, Japan. *Journal of Structural Geology*, *30*(9), 1150–1166. https://doi.org/https://doi.org/10.1016/j.jsg.2008.05.007

Keulen, N., Heilbronner, R., Stünitz, H., Boullier, A.-M. M., & Ito, H. (2007). Grain size distributions of fault rocks: A comparison between experimentally and naturally deformed granitoids. *Journal of Structural Geology*, *29*(8), 1282–1300. https://doi.org/http://dx.doi.org/10.1016/j.jsg.2007.04.003

Kirby, S. H., & Kronenberg, A. K. (1984). Deformation of clinopyroxenite: Evidence for a transition in flow mechanisms and semibrittle behavior. *Journal of Geophysical Research: Solid Earth*, *89*(B5), 3177–3192. https://doi.org/10.1029/JB089iB05p03177

Kohlstedt, D. L., & Vander Sande, J. B. (1973). Transmission electron microscopy investigation of the defect microstructure of four natural orthopyroxenes. *Contributions to Mineralogy and Petrology*, *42*(2), 169–180. https://doi.org/10.1007/BF00371506

Kollé, J. J., & Blacic, J. D. (1982). Deformation of single-crystal clinopyroxenes: 1. Mechanical twinning in diopside and hedenbergite. *Journal of Geophysical Research: Solid Earth*, *87*(B5), 4019–4034. https://doi.org/10.1029/JB087iB05p04019

Kollé, J. J., & Blacic, J. D. (1983). Deformation of single-crystal clinopyroxenes: 2. Dislocation-controlled flow processes in Hedenbergite. *Journal of Geophysical Research: Solid Earth*, *88*(B3), 2381–2393. https://doi.org/10.1029/JB088iB03p02381

Lloyd, G. E., Farmer, A. B., & Mainprice, D. (1997). Misorientation analysis and the formation and orientation of subgrain and grain boundaries. *Tectonophysics*, *279*(1), 55–78. https://doi.org/https://doi.org/10.1016/S0040-1951(97)00115-7

Markl, G., Frost, B. R., & Bucher, K. (1998). The Origin of Anorthosites and Related Rocks from the Lofoten Islands, Northern Norway: I. Field Relations and Estimation of Intrinsic Variables. *Journal of Petrology*, *39*(8), 1425–1452. https://doi.org/10.1093/petroj/39.8.1425

Matysiak, A. K., & Trepmann, C. A. (2012). Crystal–plastic deformation and recrystallization of peridotite controlled by the seismic cycle. *Tectonophysics*, *530–531*, 111–127. https://doi.org/https://doi.org/10.1016/j.tecto.2011.11.029

Menegon, L., Pennacchioni, G., Malaspina, N., Harris, K., & Wood, E. (2017). Earthquakes as Precursors of Ductile Shear Zones in the Dry and Strong Lower Crust. *Geochemistry,* *Geophysics, Geosystems*, *18*(12), 4356–4374. https://doi.org/10.1002/2017GC007189

Milke, R., Neusser, G., Kolzer, K., & Wunder, B. (2013). Very little water is necessary to make a dry solid silicate system wet. *Geology*, *41*(2), 247–250. https://doi.org/10.1130/G33674.1

Ngo, D., Huang, Y., Rosakis, A., Griffith, W. A., & Pollard, D. (2012). Off-fault tensile cracks: A link between geological fault observations, lab experiments, and dynamic rupture models. *Journal of Geophysical Research: Solid Earth*, *117*(B1), B01307. https://doi.org/10.1029/2011jb008577

Okudaira, T., Jeřábek, P., Stünitz, H., & Fusseis, F. (2015). High-temperature fracturing and subsequent grain-size-sensitive creep in lower crustal gabbros: Evidence for coseismic loading followed by creep during decaying stress in the lower crust? *Journal of Geophysical Research: Solid Earth*, *120*(5), 3119–3141. https://doi.org/10.1002/2014JB011708

Orlandini, O. F., & Mahan, K. H. (2020). Rheological evolution of a pseudotachylyte-bearing deep crustal shear zone in the western Canadian shield. *Journal of Structural Geology*, *141*, 104188. https://doi.org/https://doi.org/10.1016/j.jsg.2020.104188

Papa, S., Pennacchioni, G., Angel, R. J., & Faccenda, M. (2018). The fate of garnet during (deep-seated) coseismic frictional heating: The role of thermal shock. *Geology*, *46*(5), 471–474. https://doi.org/10.1130/G40077.1

Papa, S., Pennacchioni, G., Menegon, L., & Thielmann, M. (2020). High-stress creep preceding coseismic rupturing in amphibolite-facies ultramylonites. *Earth and Planetary Science Letters*, *541*, 116260. https://doi.org/https://doi.org/10.1016/j.epsl.2020.116260

Petley-Ragan, A., Dunkel, K. G., Austrheim, H., Ildefonse, B., & Jamtveit, B. (2018). Microstructural Records of Earthquakes in the Lower Crust and Associated Fluid-Driven Metamorphism in Plagioclase-Rich Granulites. *Journal of Geophysical Research: Solid Earth*, *123*(5), 3729–3746. https://doi.org/10.1029/2017JB015348

Petley-Ragan, A., Ben-Zion, Y., Austrheim, H., Ildefonse, B., Renard, F., & Jamtveit, B. (2019). Dynamic earthquake rupture in the lower crust. *Science Advances*, *5*(7), eaaw0913. https://doi.org/10.1126/sciadv.aaw0913

Petley-Ragan, A. J., Plümper, O., Ildefonse, B., and Jamtveit, B.: Nanoscale earthquake records preserved in plagioclase microfractures from the lower continental crust, Solid Earth, 12, 959–969, https://doi.org/10.5194/se-12-959-2021, 2021

Raleigh, C. B., & Talbot, J. L. (1967). Mechanical twinning in naturally and experimentally deformed diopside. *American Journal of Science* , *265*(2), 151–165. https://doi.org/10.2475/ajs.265.2.151

Reches, Z., & Dewers, T. A. (2005). Gouge formation by dynamic pulverization during earthquake rupture. *Earth and Planetary Science Letters*, *235*(1), 361–374. https://doi.org/https://doi.org/10.1016/j.epsl.2005.04.009

Sammis, C. G., Osborne, R. H., Anderson, J. L., Banerdt, M., & White, P. (1986). Self-similar cataclasis in the formation of fault gouge. *Pure and Applied Geophysics*, *124*(1), 53–78. https://doi.org/10.1007/BF00875719

Sibson, R. H., & Toy, V. G. (2006). The habitat of fault-generated pseudotachylyte: Presence vs. absence of friction-melt. In *Earthquakes: Radiated Energy and the Physics of Faulting* (Vol. 170, pp. 153–166). Washington, DC: AGU. https://doi.org/10.1029/170GM16

Skemer, P., & Karato, S. (2007). Effects of solute segregation on the grain-growth kinetics of orthopyroxene with implications for the deformation of the upper mantle. *Physics of the Earth and Planetary Interiors*, *164*(3), 186–196. https://doi.org/https://doi.org/10.1016/j.pepi.2007.06.011

Soda, Y., & Okudaira, T. (2018). Microstructural evidence for the deep pulverization in a lower crustal meta-anorthosite. *Terra Nova*, *30*(6), 399–405. https://doi.org/10.1111/ter.12355

Song, B. R., Johnson, S. E., Song, W. J., Gerbi, C. C., & Yates, M. G. (2020). Coseismic damage runs deep in continental strike-slip faults. *Earth and Planetary Science Letters*, *539*, 116226. https://doi.org/https://doi.org/10.1016/j.epsl.2020.116226

Stünitz, Holger, Keulen, N., Hirose, T., & Heilbronner, R. (2010). Grain size distribution and microstructures of experimentally sheared granitoid gouge at coseismic slip rates – Criteria to distinguish seismic and aseismic faults? *Journal of Structural Geology*, *32*(1), 59–69. https://doi.org/http://dx.doi.org/10.1016/j.jsg.2009.08.002

Sullivan, W. A., & Peterman, E. M. (2017). Pulverized granite at the brittle-ductile transition: An example from the Kellyland fault zone, eastern Maine, U.S.A. *Journal of Structural Geology*, *101*, 109–123. https://doi.org/https://doi.org/10.1016/j.jsg.2017.07.002

Trepmann, C. A., & Stöckhert, B. (2013). Short-wavelength undulatory extinction in quartz recording coseismic deformation in the middle crust; An experimental study. *Solid Earth*, *4*(2), 263–276. https://doi.org/10.5194/se-4-263-2013

Trepmann, C. A., Renner, J., & Druiventak, A. (2013). Experimental deformation and recrystallization of olivine-processes and timescales of damage healing during postseismic relaxation at mantle depths. *Solid Earth*, *4*(2), 423–450. https://doi.org/10.5194/se-4-423-2013

Trepmann, C. A., & Seybold, L. (2019). Deformation at low and high stress-loading rates. *Geoscience Frontiers*, *10*(1), 43–54. https://doi.org/https://doi.org/10.1016/j.gsf.2018.05.002

Trepmann, Claudia A, & Stöckhert, B. (2002). Cataclastic deformation of garnet: a record of synseismic loading and postseismic creep. *Journal of Structural Geology*, *24*(11), 1845–1856. https://doi.org/https://doi.org/10.1016/S0191-8141(02)00004-4

Wilson, B., Dewers, T., Reches, Z., & Brune, J. (2005). Particle size and energetics of gouge from earthquake rupture zones. *Nature*, *434*(7034), 749–752. https://doi.org/10.1038/nature03433

Xu, S., & Ben-Zion, Y. (2017). Theoretical constraints on dynamic pulverization of fault zone rocks. *Geophysical Journal International*, *209*(1), 282–296. https://doi.org/10.1093/gji/ggx033

Yuan, F., Prakash, V., & Tullis, T. (2011). Origin of pulverized rocks during earthquake fault rupture. *Journal of Geophysical Research: Solid Earth*, *116*(B6). https://doi.org/10.1029/2010JB007721

[Journal of Geophysical Research: Solid Earth]

Supporting Information for

High stress deformation and short-term thermal pulse preserved in exhumed lower crustal seismogenic faults (Lofoten, Norway)

Campbell, L. R[1]. & Menegon, L.[2]

[1]Department of Geography, Geology and Environment, University of Hull, Hull HU6 7RX

[2]The Njord Centre, Department of Geosciences, University of Oslo, P.O. Box 1048, Blindern, Norway

Contents of this file

Figures S1 to S5

Introduction

The following supporting figures offer additional examples or analysis to support those in the main manuscript. All relevant methods are described in the main manuscript.

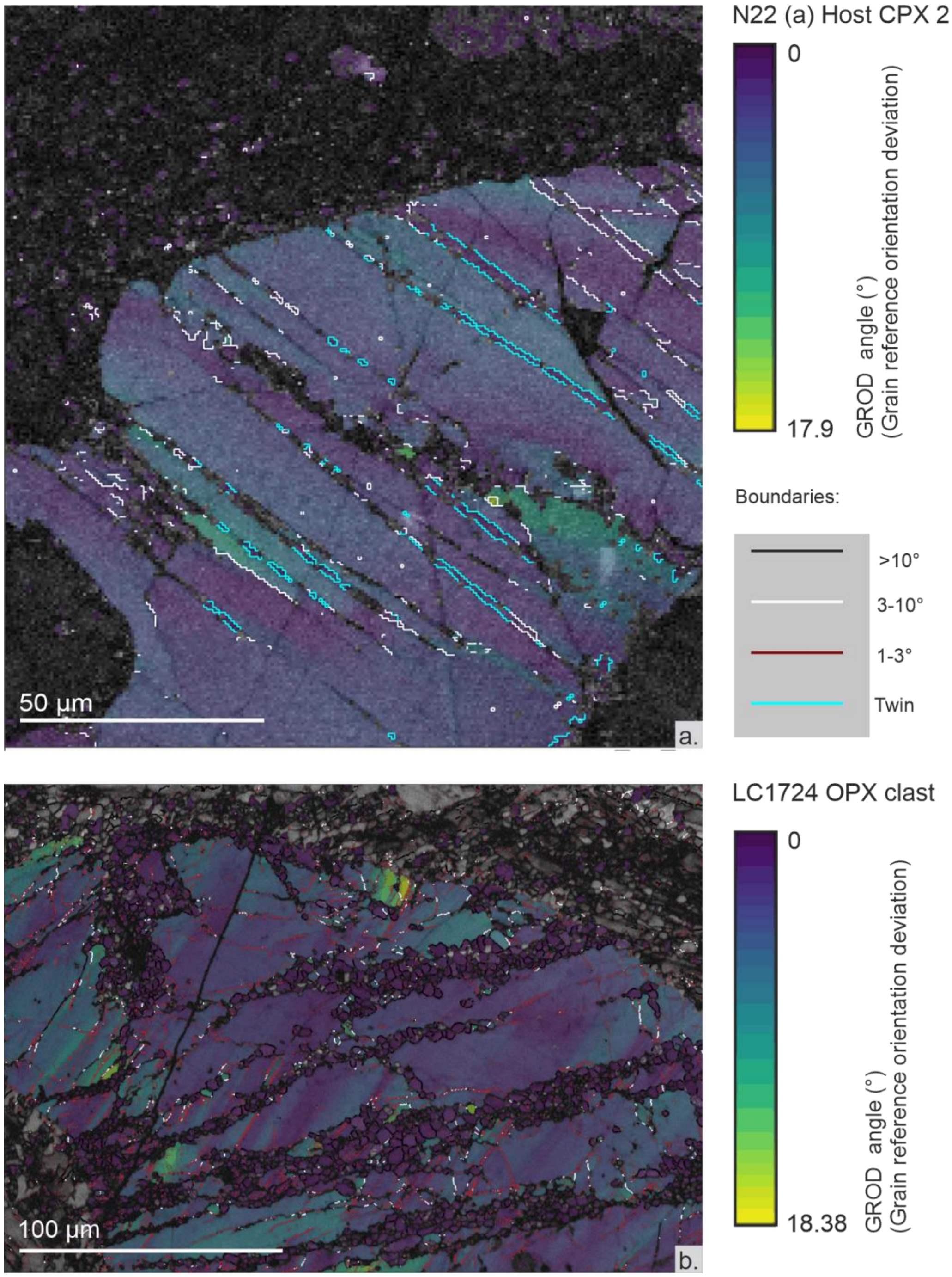

Figure S1. Grain reference orientation deviation (GROD) maps showing misorientation of points from the grain's mean orientation. **a)** GROD map of 'Host CPX 2' (see Fig. 3 f-g); **b)** GROD map of OPX clast (see Fig. 8).

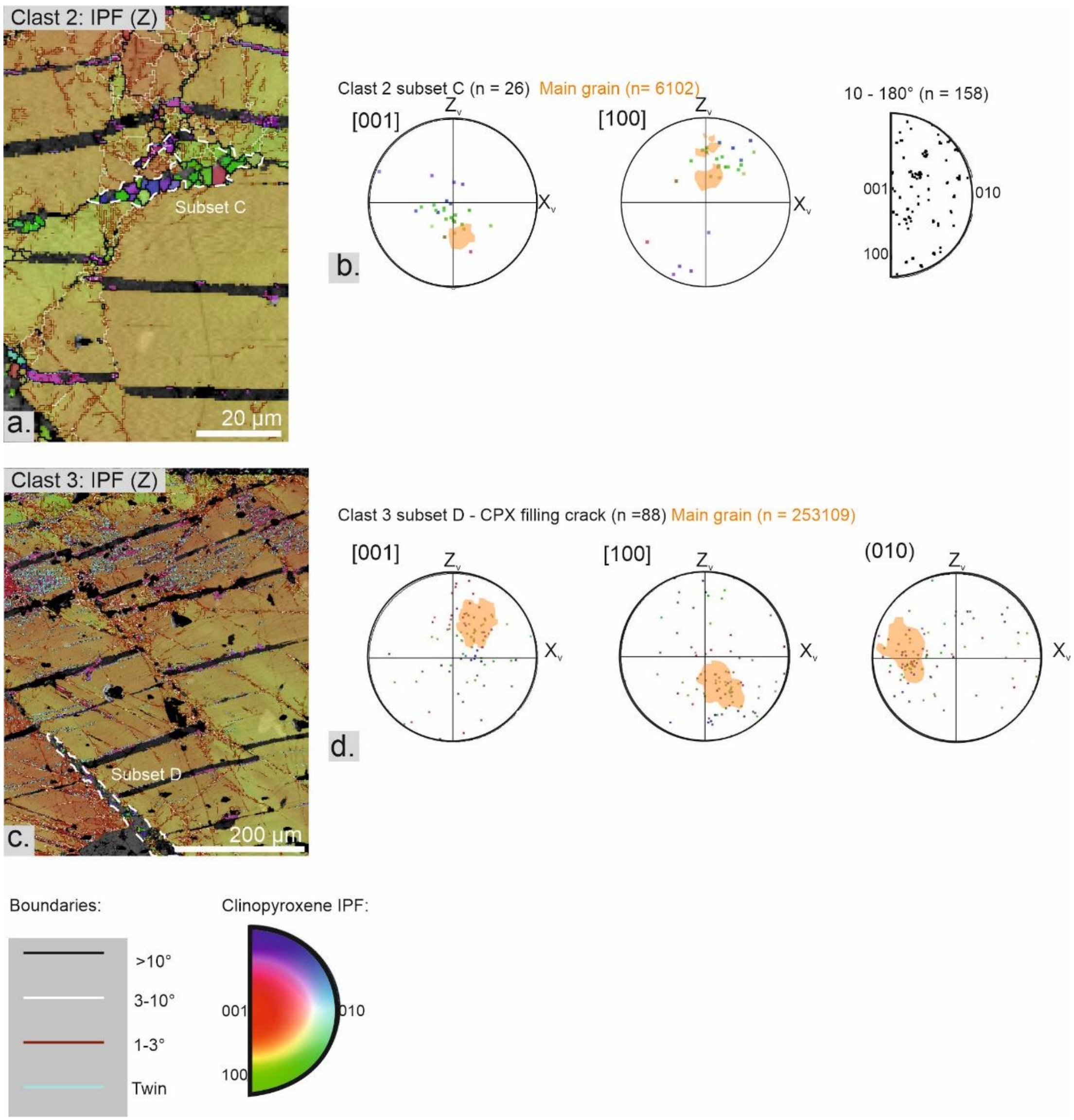

Figure S2. fine-grained clinopyroxene observed in clasts **a)** IPF (Z) map for clinopyroxene in clast 2; **b)** pole figures with IPF (Z) colouring and rotation axes in crystal co-ordinates for fine-grained CPX filling a crack in clast 2 (1 point per grain), points from main grain shown in orange overlay; **c)** IPF (Z) map for clinopyroxene in clast 3; **d)** pole figures for fine-grained CPX filling crack in clast 3 (1 point per grain), points from main grain shown in orange overlay.

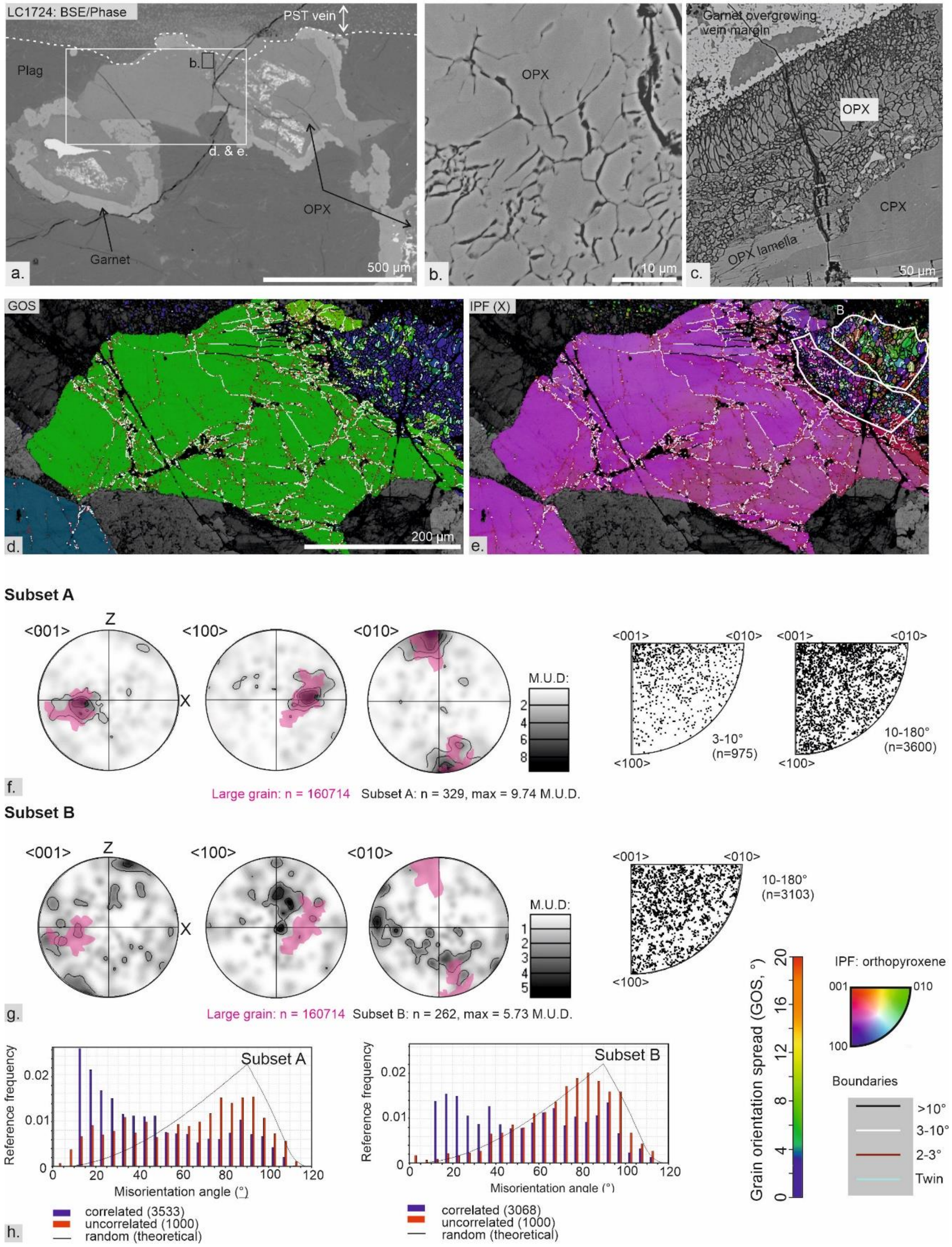

Figure S3. Additional examples of deformed orthopyroxene. **a)** BSE image of orthopyroxene grain bordering pseudotachylyte vein in sample LC1724, and adjacent pseudotachylyte vein, with adjacent phases and location of EBSD analysed region labelled; **b)** high magnification BSE image of pervasively fragmented region of orthopyroxene grain shown in a); **c)** fragmentation of orthopyroxene lamellae within a clinopyroxene grain bordering a pseudotachylyte vein in N22. This forms part of a large polycrystalline clast surrounded by PST (location shown in Fig. 2f); **d)** EBSD GOS map of OPX in the host rock bordering a PST vein, LC1724 (location indicated in a)); **e)** IPF (X) orientation map of OPX; **f)** pole figures (lower hemisphere, equal area) & rotation axes (in crystal co-ordinates) for subset A in the fragmented part of the grain(s) – subset location shown in b). The pink areas in the pole figures represent the orientation of the host opx grain; **g)** pole figures (lower hemisphere, equal area) & rotation axes (in crystal co-ordinates) for subset B in the fragmented part of the grain(s) – subset location shown in b). The pink areas in the pole figures represent the orientation of the host opx grain; **h)** misorientation histograms for subset A and subset B.

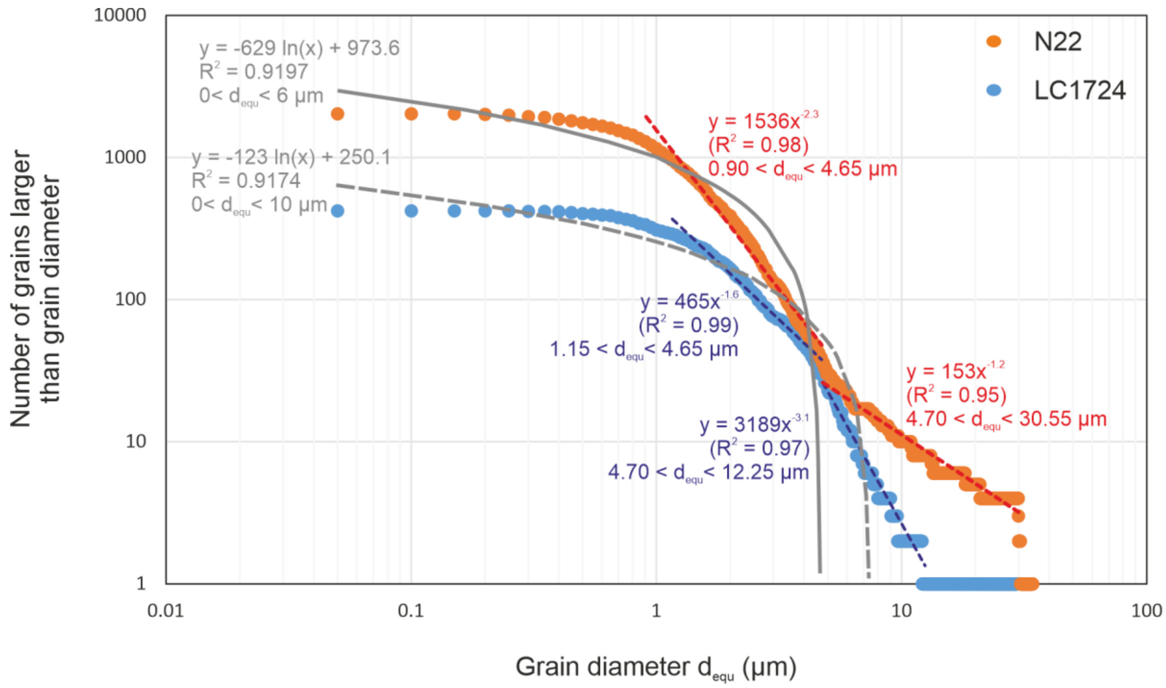

Figure S4. Grain size distribution (GSD) for fragmented orthopyroxene in vein margins for samples N22 and LC1724. Best fit lines are shown for log normal (grey) and power law (red/blue) distributions.

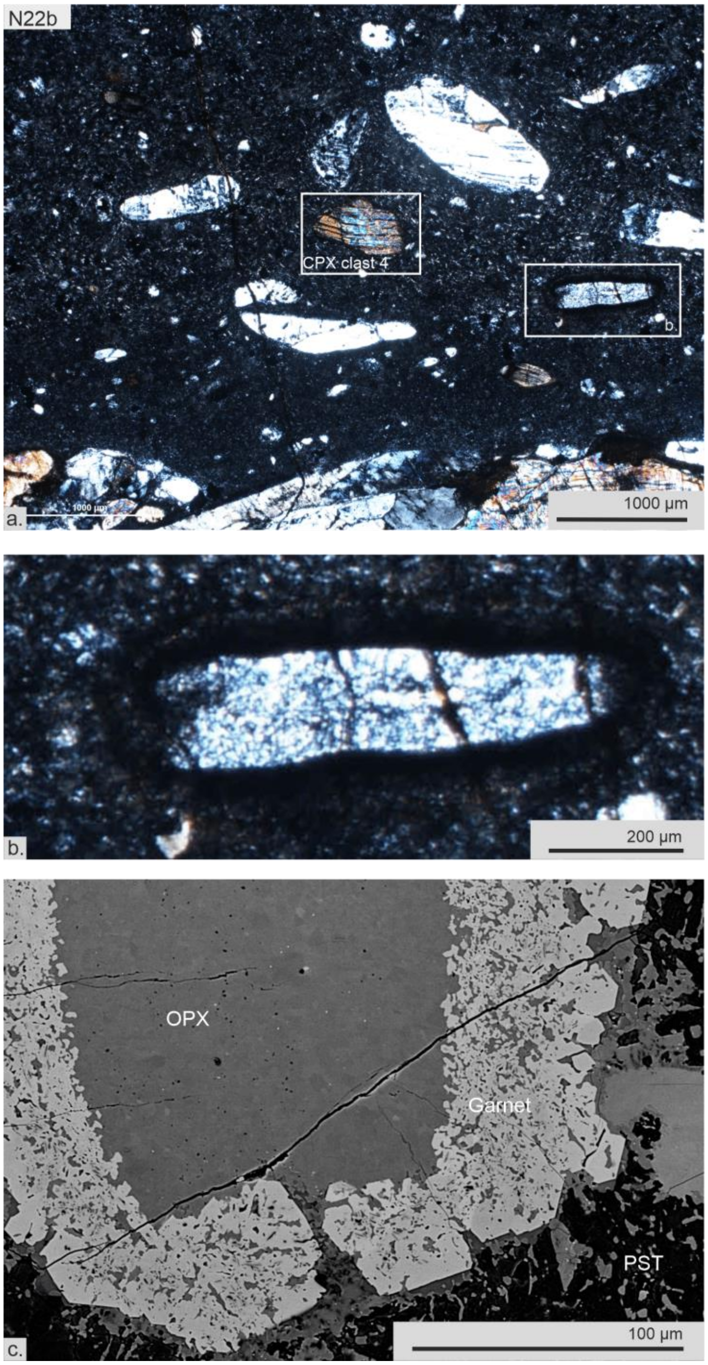

Figure S5. Fragmented OPX clast: **a)** Optical micrograph (XPL) showing position of clast in thin section N22b relative to CPX clast 4. Fragmentation of the OPX can be seen in the mixed extinction of the OPX; **b)** close-up image of same clast, (XPL) ; **c)** BSE image of part of same clast, showing fragmentation in the OPX and the garnet rim.